JOINT EUROPEAN TORUS JET

JET-R(90)03

G. Gorini and N. Gottardi

Inversion Methods for Analysis of Neutron Brightness Measurements in Tokamaks

Inversion Methods for Analysis of Neutron Brightness Measurements in Tokamaks

G. Gorini[1] and N. Gottardi

JET Joint Undertaking, Culham Science Centre, OX14 3DB, Abingdon, UK

[1]*Present address: Istituto di Fisica del Plasma, Associazione Euratom-ENEA-CNR, Milano, Italy*

ABSTRACT

The problem of determining the neutron emissivity from neutron brightness measurements in magnetic fusion plasmas is addressed. In the case of two-dimensional measurements with two orthogonal cameras, a complete, tomographic analysis of the data can in principle be performed. The results depend critically on the accuracy of the measurements and alternative solutions can be. sought under the assumption of a known emissivity topology (Generalized Abel Inversion). In this work, neutron brightness data from the JET tokamak have been studied with both methods. We find that with the present experimental uncertainty (levels 10-20%) the Abel inversion method works best, while two-dimensional information cannot in general be deduced. This is confirmed by studies of the error propagation in the inversion using artificial data, which are also presented here.

An important application of emissivity profile information is the determination of the plasma deuterium temperature profile, $T_D(R)$. Results are presented here from the analysis of JET data and the errors in $T_D(R)$ are discussed in some detail. It is found that, for typical JET plasma conditions, the dominant source of uncertainty arises from the high plasma impurity level and the fact that it is poorly known; these problems can be expected to be remedied and neutron brightness measurements would be ex pected to be very effective (especially in high density plasmas) as a $T_D(R)$ diagnostics.

1. Introduction

As magnetically confined plasmas achieve conditions approaching ignition, higher fusion rates are obtained and new neutron diagnostic measurements become possible. The JET machine is an example of such plasma physics experiments allowing for new neutron diagnostics to be tested. These measurements are at present in many respects a complement to other diagnostic data. However, future experiments using D-T plasmas are expected to depend critically on neutron based information, and better neutron measurements are also being proposed which take full advantage of the expected high fusion rates [1]. It is therefore of interest to discuss in some detail what kind of information one can deduce from fusion neutron measurements. This can be done by studying the data from present experiments. An example of such new data come from measurements of the line-integrated neutron emissivity of the plasma, i.e., the neutron brightness. The purpose of this paper is to study the methods that can be used in the analysis of neutron brightness data, i.e., the inversion of the data to determine the plasma neutron emissivity. Furthermore, the emissivity profile can, under certain conditions, be used to deduce other types of information on the plasma, for instance, the ion temperature profile. This is also part of this paper.

Neutron brightness measurements have recently been performed for the first time in the JET machine [2]. They were obtained with two multichannel collimator arrays (neutron cameras) viewing the plasma in the poloidal plane through a vertical and horizontal port of the machine. These collimators define a number of lines of sight through the plasma (Fig.1) along which the neutron brightness is measured. Since two cameras are used, it is in principle possible to determine the two-dimensional radial

distribution of the emissivity: this procedure is known as neutron tomography.

The problem of deducing a local quantity from line-integrated data is common to diagnostic techniques used in other fields of science. It entails the inversion of the integral equation

$$f(p,\varphi) = \int_{L(p,\varphi)} g(r,\theta) \; dL \qquad (1)$$

where $g(r,\theta)$ is a local quantity (i.e., the neutron emissivity in our case) to be determined from $f(p,\varphi)$, its line-integral (brightness) along the viewing line, $L(p,\varphi)$; (p,φ) and (r,θ) are polar coordinates (see Fig.2). The inversions of line-integrated measurements such as expressed by Eq.1 are common to tomography (as originally used in medical diagnostics) and to diagnostics of tokamak fusion plasmas such as JET [3-7].

Several methods can be attempted for the analysis of line-integrated data. The methods used in each case depend on completeness and quality of the data which in turn determine how much external information and which constraints must be used in the analysis. For instance, the interferometric measurement of the line-integrated electron density [4] is made with a single camera. In this case, the analysis of the data must use additional information on the density contours of the plasma which are usually assumed to be the magnetic flux contours for the identified plasma equilibrium; this method of analysis is a generalization of the Abel inversion. Other diagnostics make use of two cameras, like the soft X-ray measurements in JET [3]. In this case, the quality of the experimental data is very high and this has made it possible to perform a complete, two-dimensional

(tomographic) imaging of the plasma cross section. The tomographic approach, too, involves some assumptions, mainly because the two-dimensional profile is not uniquely determined by the finite data set. However in this case it is sufficient to assume that no profile features are finer than the radial and poloidal resolution of the detection system. The neutron brightness measurements in JET are somewhat intermediate to these two cases : these measurements are made with two cameras, but the number of lines of sight is small and the experimental uncertainties are non-negligible. Therefore, it is not a priori clear whether they can be made the object of a two-dimensional tomographic analysis. Instead, it may be preferable to make use of the fact that the emissivity contours are the same as the magnetic flux contours, and make combined use of the data from the two cameras to obtain a more accurate determination of the radial emissivity profile.

In order to study the problem of how to make best use of data from neutron brightness measurements in tokamaks, we have performed a detailed comparison of the two methods of analysis, which represent extreme cases with regard to the number of assumptions involved. The first method is Cormack tomography (Sect.3). In plasma diagnostics, this tomography algorithm is well known for its application to soft X-ray data in JET [3]. The second method is a generalized Abel inversion (Sect.4), which has already been used at JET for the analysis of electron density and of bolometric measurements [4,5]. Both methods have here been applied to neutron brightness data for the JET plasma, with examples representing different shapes of emissivity profiles. However, a significant test of the applicability of the methods is possible only if the emissivity profile resulting from the analysis is known *a priori*. For this reason artificial brightness data were also anal-

ysed with the two inversion methods. These data were obtained by line integration of known emissivity profiles; the same data were also perturbed in a way simulating the experimental uncertainties. The results of the analysis of unperturbed and perturbed artificial data illustrate the sensitivity of the two inversion methods to the experimental uncertainties. More generally, these results indicate what is the best use of neutron brightness data in tokamaks.

An important application of neutron emissivity profile information is the determination of the plasma deuterium temperature profile, $T_D(R)$, where R is the radial coordinate (major radius) in the plasma equatorial plane (we use this coordinate for consistency with other plasma temperature measurements). More precisely, the neutron emissivity g in a Maxwellian deuterium plasma is a well-known function of T_D and of the deuterium density n_D,

$$g = \frac{1}{2} n_D^2 < \sigma v > \qquad (2)$$

Here $<\sigma v>$ is the plasma reactivity (averaged over a Maxwellian deuterium velocity distribution) which is a steep function of T_D [8]. One can therefore derive the $T_D(R)$ profile from g(R) provided that the $n_D(R)$ profile is also known and that the ion velocity distribution is Maxwellian. These requirements limit considerably the diagnostic application of the neutron emissivity in the case of JET plasmas: the latter assumption is generally not satisfied when deuterium neutral beam injection is used for heating the plasma. Another limitation is due to the fact that the deuterium density has to be derived from the electron density profile and the impurity content; for

typical JET plasma conditions, the impurity content is not very well known. Nevertheless, $T_D(R)$ profiles from JET neutron brightness measurements can be obtained for cases where the plasma impurity content was low, and the accuracy and the space and time resolution are comparable to those of other $T_D(R)$ diagnostic methods. This is a significant advancement over previous results which were based on the volume integrated neutron emission to derive the central deuterium temperature or density in JET Ohmic and ICRH heated plasmas [9]. In the latter case, the results were subject to the assumption that the ion and electron temperature profiles had similar shapes apart from a scale factor represented by their central value. This assumption can here be tested directly on the $T_D(R)$ profiles derived. Other applications of the neutron brightness data, and in particular the imaging of plasmas with neutral beam injection, are not discussed in this paper.

2. Experimental

The total neutron emission of a deuterium plasma in JET is typically between 10^{12} and 10^{16} neutrons s^{-1} depending on the type of discharge. The neutrons come from the reaction $D+D \rightarrow {}^3He+n$ and have a characteristic energy of 2.45 MeV. More precisely, the energy spectrum of these neutrons is Gaussian in the case of Maxwellian plasmas, with a width depending on the ion temperature which is measured directly with different spectrometers [10-11]. The neutron emissivity profile of the plasma is measured with a system of two neutron cameras, and below we describe some features of the measurement of relevance to this analysis.

The neutrons passing the multicollimators are detected with NE213 liquid scintillators coupled to photomultipliers. The neutrons passing the multicollimators are detected with NE213 liquid scintillators coupled to

photomultipliers. There are two types of background effects in the measurement: backscattered neutrons from the vessel walls, and γ-rays from neutron activation reactions in the machine. Their influence has been considerably reduced in these measurements by applying energy and pulse shape discrimination to the detection signals. Pulse Shape Discrimination (PSD) is a well known technique [12] for the rejection of γ-ray events. It is based on the differentiation of neutron- and γ-induced pulses in the scintillator, where the neutron pulses have shorter rise times than those induced by γ-rays. In order to reject the backscattered (energy degraded) neutrons, a discrimination threshold of about 2.0 MeV is applied to the measured continuous proton recoil pulse height spectrum. While the PSD is normally effective in rejecting γ-ray events, a residual fraction of background neutrons is always present in the measured neutron fluxes, amounting tipically to a few percent of the peak neutron brightness. It is roughly the same, in absolute terms, for all data channels as judged from estimates based on neutron transport calculations [13]. This means that while the background contribution to the data is a few percent for a central line of sight if the profile is peaked, it is higher for broad profiles and for peripheral lines of sight. In fact, there are cases when the neutron emission is very localised in the plasma centre so that the most peripheral channels probably see only background neutrons. These cases gave an experimental confirmation (with an uncertainty of ±20%) of the background flux estimate based on neutron transport calculations; the estimated background corresponding to the 2.0 MeV threshold was therefore subtracted from the measured brightness profiles prior to analysis.

An accurate determination of the neutron detection efficiency of each detector in the two cameras is essential for the profile measurement. Typi-

cally, the detection efficiency is about 2.5% for 2.45 MeV neutrons using the energy threshold mentioned above. This value was determined for each detector in calibration measurements, which resulted in a relative precision (between the data channels) of ±10% and about ±15% in absolute terms. The absolute accuracy of the neutron emissivity determination can be checked in an overall way by comparison with the total neutron emission measured with a set of fission chambers located around the tokamak [14]with an accuracy of ±10%.

Other figures of merit of the camera system are space and time resolution. The spatial resolution is determined by two factors, namely the aperture of each collimator channel (the viewing area is typically ±11 cm wide in the central region of the plasma), and the distance between two adjacent channels (which is about 22 cm); because of the finite poloidal width of the lines of sight, a reduction of the experimental data is necessary, as discussed below. The time resolution depends on the source strength through the counting statistics that can be achieved. Typically, one or a few seconds integration time (i.e. almost the entire flat top of the plasma current) is required in the case of Ohmic discharges in order to achieve a counting statistics of about 50 counts in the peripheral channels, while 50 ms can be sufficient for additionally heated discharges. This is illustrated by the two examples of extreme profile shapes of Fig.3, where the brightness data are plotted vs channel number. Fig.3a shows an example of a very peaked brightness profile obtained in a plasma discharge with ICRF heating after the injection of a deuterium pellet (the time traces of some relevant plasma parameters are shown in Fig.4). The integration time was 100 ms which gave a counting statistics ranging from 250 to over 16000 counts for the channels of the horizontal camera and from 40 to over 6400 counts for the

vertical one; these probably represent the highest possible count rates that can be achieved without suffering from dead time effects or from deterioration of the rejection of γ-ray events. The counting statistics limitation is encountered for the peripheral channels, the use of which is anyway hampered by background neutrons. The other example is a very broad brightness profile (Fig.3b) and was obtained by time integration over the entire current flat top (7 s) of a 4 MA Ohmic discharge. In this case, the counting statistics ranged from 160 to 2400 counts for the horizontal camera and from 17 to 470 for the vertical one. Although, in the case of Ohmic discharges, the integration times are rather long, the assumption of steady state plasma conditions is well satisfied, apart from the occurrence of sawtooth instabilities.

The two neutron brightness profiles of Fig.3 represent reduced data since this is required by the analysis procedure. More precisely, the data have been reduced so that they represent the brightness values as they would have been measured along the same collimation lines but of infinitely small poloidal width. If the latter was true, the neutron flux at each detector would be

$$F(p,\varphi) = \frac{(A_{ap})^2 \eta}{4\pi d^2} f(p,\varphi) \qquad (3)$$

where A_{ap} is the aperture area and d is the length of the collimator, η is an attenuation factor (taking into account the presence of material obstructions along the line of sight), and $f(p,\varphi)$ is the neutron brightness corresponding to the collimator axis $L(p,\varphi)$ (see Fig.2). Since the collimator apertures are not small, $f(p,\varphi)$ in Eq.3 must be replaced by the brightness value

$\langle f(p,\varphi)\rangle$ averaged over the viewing area (see Fig.5). The difference between $f(p,\varphi)$ and $\langle f(p,\varphi)\rangle$ depends on the collimation geometry and on the emissivity profile shape and has to be determined numerically. For an estimate of this difference we used the collimation geometry of Fig.5 and the profile shape of an initial inversion (i.e., using $\langle f(p,\varphi)\rangle$ in place of $f(p,\varphi)$ in Eq.1). The resulting difference between $f(p,\varphi)$ and $\langle f(p,\varphi)\rangle$ was about 10% for the peripheral channels and less than 1% for the central channels. This correction was applied to the data although it is small compared to other larger sources of uncertainty in the data.

For the analysis, we use other experimental data as an input in this work. These are i) the magnetic flux surfaces and ii) the electron density and Z_{eff}.

i) The magnetic flux surfaces result from the identification of the magnetic equilibrium of JET plasmas [15]. This corresponds to the solutions to the Grad-Shafranov equation which are determined by fits to data of the magnetic measurements. For the plasma discharges studied in this work, these magnetic measurements were performed with a set of 14 poloidal flux loops and 18 pick-up coils around the plasma. Moreover the diamagnetism of the plasma, which was determined with a diamagnetic flux loop, was used as an additional constraint on the equilibrium solution [16]. The resulting magnetic flux surfaces (i.e., nested toroidal surfaces generated by the magnetic field lines) are believed to be surfaces of constant temperature and density, and could therefore be used as neutron emissivity contours if the plasma ion distribution is Maxwellian. The uncertainty in the identification of the flux surfaces depends on the number of measuremed data points that are fitted and on the shape of plasma current profile; e.g., the

radial position of the magnetic axis is known to ±5 cm, while the elongation of the innermost surfaces has a typical uncertainty of ±10%.

ii) The electron density profile in JET plasmas is measured by two diagnostics, namely the LIDAR Thompson scattering system [17] (providing n_e at 50 points along a horizontal chord) and the far-infrared interferometer [18]. The latter measures the line-integrated electron density along 6 chords, which is inverted with a Generalized Abel Inversion of the type described in Sect.4. This leads to results on the density profile with local uncertainties of about ±10% as detemined by direct comparison of the two measurements [5]. The effective ion charge (Z_{eff}) is derived from the measured line-integrated visible continuum emission (bremstrahlung). Although the 15-chord measurement provides space resolved data [7], here we only make use of the chordal-average value for Z_{eff} and discuss the sensitivity of neglecting Z_{eff} profile effects. From the Z_{eff} value, and from the spectroscopic evidence that carbon is the main impurity in JET ([19]), one can derive the ratio between the deuteron and electron density n_D/n_e needed for our analysis. Moreover, the shape of the electron density profile is also used. For the present analysis of the experimental neutron brightness profiles of Fig.3 we used $n_e(R)$ of Fig.6 while the Z_{eff} value was 2.3 and 2.5 for the peaked and the broad profile, respectively. In the latter case the deuteron density was further corrected relative to n_e because of the use of a ^3He admixture in the plasma (taken as part of Z_{eff} in addition to carbon); this gave a density ratio of $n_D/n_e=0.45$. From the electron density profile and the n_D/n_e ratio, the deuterium density profile was finally deduced, which in turn was used to derive the T_D profile from the neutron emissivity.

3. Cormack Tomography

A detailed description of Cormack Tomography can be found in the original articles [20] or in Ref.[2]. Here we summarize the principles of its application to neutron brightness measurements.

From a mathematical point of view, Cormack Tomography is a solution to Eq.1 in the form of a series expansion. The neutron emitting region (i.e., the region where $g(r,\theta)$ is different from zero) is assumed to be contained within a circle with a radius normalized to unity. The functions $g(r,\theta)$ and $f(p,\varphi)$ in Eq.1 can be expanded in the Fourier series:

$$g(r,\theta) = \sum_{m=-\infty}^{+\infty} g_m(r) e^{-im\theta} \tag{4}$$

$$f(p,\varphi) = \sum_{m=-\infty}^{+\infty} f_m(p) e^{-im\varphi} \tag{5}$$

where

$$g_m(r) = \frac{1}{2\pi} \int_0^{2\pi} g(r,\theta)\ e^{im\theta}\ d\theta \tag{6}$$

$$f_m(p) = \frac{1}{2\pi} \int_0^{2\pi} f(p,\varphi)\ e^{im\varphi}\ d\varphi \tag{7}$$

Inserted in Eq.1, each mode m is obtained as

$$f_m(p) = 2 \int_p^1 \frac{g_m(r)\, T_m\left(\frac{p}{r}\right) r}{\sqrt{r^2 - p^2}}\ dr \tag{8}$$

and has the solution

$$g_m(r) = -\frac{1}{\pi} \frac{d}{dr} \int_r^1 \frac{f_m(p)\, T_m\left(\frac{p}{r}\right)}{p\sqrt{r^2 - p^2}}\ dp \tag{9}$$

where $T_m(z)=\cos(m\ \cos^{-1}z)$ is a Tschebysheff polynomial of the first kind of degree m in z. Notice that, for m=0, this solution is equivalent to an Abel inversion (see next section).

In principle, Eq.9 is a solution to the inversion problem. However, it is of little practical interest for our application to neutron brightness data. Instead of using Eq.9, it is better to use the analytical solution of Eq.8 developed by Cormack in the form of an elegant series expansion. When $f_m(p)$ is expanded in the following form,

$$f_m(p) = 2\sum_{l=0}^{\infty} a^l_m \sin\left[(m+2l+1)\cos^{-1}p\right] \tag{10}$$

then the corresponding expansion of $g_m(r)$ is

$$g_m(r) = \sum_{l=0}^{\infty} (m+2l+1)\ a^l_m\ R^l_m(r) \tag{11}$$

where $R^l_m(r)$ is a Zernicke polynomial defined as

$$R^l_m(r) = \sum_{s=0}^{l} \frac{(-)^s\,(m+2l-s)!\ r^{m+2l-2s}}{s!\,(m+l-s)!\,(l-s)!} \tag{12}$$

The inversion problem is then reduced to the determination of the coefficients a^l_m. Notice that in order to resolve the m^{th} poloidal harmonic in the emissivity, it is sufficient to know the m^{th} harmonic of the measured brightness. In other words, the original, two-dimensional inversion problem is reduced into solving a number of one-dimensional problems. In general, the number of poloidal harmonics that can be determined is limited by the resolution of the measurement. In the case of a two-camera system with fan-like geometry like the one at JET, $f(p,\varphi)$ is effectively sampled at 4 values of φ as

shown in Fig.7, where the location of the experimental chords in the (p,φ) plane are seen to be aligned along 4 lines of approximately constant φ. This means that the measurement can identify only 4 harmonics of the neutron brightness and hence 4 poloidal harmonics of the emissivity. In this work we choose the m=0, $\sin\theta$, $\cos\theta$ and $\cos 2\theta$ harmonics, which should adequately represent the poloidal shape of the neutron emissivity. The choice of the maximum l value to be used in the expansion is also limited by the radial resolution of the system. A number of auxiliary lines of sight with zero brightness must be added to the experimental brightness data in order to avoid arbitrary fluctuations of the solution near the unit circle (see Fig.7). Finally, the coefficients a^l_m are determined with a least-sqare fit to the experimental and auxiliary data. An example of this fit is shown in Fig.8 where the fitted brightness $f(p,\varphi)$ is plotted along with the experimental data of Fig.3a. The corresponding neutron emissivity profile is shown in Fig.9.

4. Generalized Abel Inversion

If the emissivity contours were concentric circles, only the poloidal m=0 components of Eq.4 and 5 would be needed for a complete solution of the problem. In this case the inversion of Eq.1 is called Abel inversion and can be performed in many ways. Moreover, the Abel inversion can be generalized and such a method has been developed for the JET plasma, which is generally non-circular. The method is called Generalized Abel Inversion; it is a generalization of the Abel inversion in the sense that knowledge is required about the emissivity contours, albeit these do not have to be circular. In fact, in this work we use the magnetic flux surfaces as emissivity contours. This allows us to project the data (as is described below) so that a comparison of the data from the two cameras can be made. In this way we

can both test the procedure and the consistency of the two data sets and make combined use of them if desired.

The 19 lines of sight of the horizontal and vertical neutron cameras (L_1-L_{10} and L_{11}-L_{19}) are tangents to a set of magnetic flux surfaces (S_1-S_{19}). For the projection, the area between two such adjacent surfaces is taken as a resolution element, or pixel, and the emissivity g is assumed to be constant within each pixel. Fig.10 shows the principles of this representation for a simplified system consisting of 5 channels. If we denote by M_{ij} the length of the line of sight L_i inside the j^{th} pixel, where the emissivity is g_j, we then have

$$f_i = \sum_{j=1}^{19} M_{ij}\, g_j \qquad (13)$$

where f_i is the brightness corresponding to the line L_i.

Let us now consider a virtual set of vertical lines of sight V_k tangential to the same set of pixels: there are in fact two sets of these lines, V^R_k and V^L_k, respectively to the right and to the left of the magnetic axis. The virtual brightnesses along the lines V^R_k, which we denote f^R_k, can now be determined and are given by

$$f^R_k = \sum_{j=1}^{19} N^R_{kj}\, g_j \qquad (14)$$

where N^R_{kj} is the length of V^R_k inside the j^{th} pixel. The relationship between the virtual and experimental brightness distribution can be expressed by the matrix equation

$$\mathbf{f}^R = \mathbf{N}^R\, \mathbf{M}^{-1}\, \mathbf{f} \qquad (15)$$

A similar expression can be derived for $\mathbf{f}^L$, the brightnesses along the lines V^L_k. The 19+19 virtual brightness values, $\mathbf{f}^R$ and $\mathbf{f}^L$, are the projected data. These data should form one smooth curve if the assumption of constant emissivity on magnetic flux surfaces was correct apart from deviations due to experimental errors in the brightness values or uncertainties in the magnetic flux surfaces. We also note that the magnetic surfaces can be shifted relative to the surfaces of constant pressure (due, for instance, to pressure anisotropy), and hence relative to the neutron emissivity contours. However such effects are difficult to measure directly because they usually are of the same magnitude as the experimental uncertainties. This is illustrated in Fig.11.

Fig.11 shows the virtual brightness profile for the vertical neutron camera obtained from the experimental profile of Fig.3a. In this case the radial position of the flux surfaces needed correction (see Fig.12) in order to obtain consistency between the assumed emissivity contours and the neutron brightness profile from the vertical camera. This problem may be interesting in itself, but in the present study it is considered merely as part of the uncertainties of the analysis. What is important to note is that the global position correction made is generally sufficient for obtaining consistency between the brightness measurements and the magnetic topology, allowing one to procede with the inversion of the profile data.

If the projected data are internally consistent, it is possible to find a smooth profile that fits the data. An example of such a fit and of the subsequent steps of the inversion procedure are shown in Fig.13. The fit to the brightness profile can be inverted to give the emissivity profile, using the same matrix formalism as in Eq.13, albeit with an arbitrary number of virtual chords. In fact, the fitted brightness profile consists of two parts (f^R

and f^L, see Fig.13c), one for each side of the magnetic axis. These two parts can be inverted separately, and two emissivity profiles (g^R and g^L), are obtained, which were finally averaged to give the neutron emissivity profile shown in Fig.13d.

5. Comparison of the inversion methods

To illustrate the information that can be extracted from neutron brightness data, the Cormack Tomography and the Generalized Abel Inversion were applied to the same profiles. We chose the two experimental profiles of Fig.3 (representing the inversion of two extreme profile shapes), and four artificial brightness profiles. The latter consisted of i) two artificial profiles with shapes similar to the experimental ones, obtained by integration of analytic T_D and n_D profiles, and ii) the same profiles after a random perturbation reproducing the scatter observed in the experimental data. These artificial profiles allowed us a better separation of the effects on the analysis due to the profile shape and the uncertainties in the data. More precisely, the inversion of the unperturbed profiles using both methods allowed a test of the results under conditions of negligible experimental uncertainties; the reliability of a result was judged simply by comparison between the deduced and original neutron emissivity profiles. The sensitivity to experimental errors was then estimated by inverting the perturbed brightness profiles. The results of the inversion of the mentioned six brightness profiles using the Cormack Tomography and the Generalized Abel Inversion are presented below.

a) Peaked Profiles

A direct comparison of inversion results for the peaked neutron brightness profile of Fig.3a is shown in Fig.14. This shows that the emissivity

profiles on the plasma equatorial plane obtained with Cormack Tomography and Generalized Abel Inversion methods are in rather poor agreement. Moreover, the emissivity contours determined by the tomography method (Fig.15) do not fit very well with the magnetic flux surfaces. This suggests that the tomography result may not be reliable in the presence of oscillations towards the plasma edge in the fitted brightness profile (Fig.8b) and, consequently, in the emissivity profile (Figs.9,14). These oscillations are a result of the polynomial fit of the data, but their magnitude is rather large in this case. It should be noted that an error in the background subtraction is not a likely cause for these oscillations, but they may rather arise from the relative uncertainties in the data of the central data channels (see below).

The inversion of the two peaked artificial brightness profiles (Figs.16-23) indicates that the relative uncertainties in the brightness data are the likely cause for the inaccuracy of the results of the Cormack Tomography. In fact, when no random perturbation is applied to the profile, both inversion methods give good results. This is shown for instance in Fig.17 where the emissivity contours determined by the Cormack Tomography method agree nicely with the original emissivity contours (which are the magnetic flux surfaces). Also the edge oscillations in the fitted brightness profile (Fig.16) are small. The generalized Abel Inversion gives very good results, reproducing the input emissivity profile over four orders of magnitude (Fig.18). The comparison of the emissivity profiles in the equatorial plane determined with the two methods (Fig.19) shows that the tomography result is accurate over about two orders of magnitude of the emissivity. Thus the Abel inversion seems to have a wider range over which the reconstruction of the radial emissivity profile can be made; this is believed to be a conse-

quence of the consistent interpolation of the data made before the inversion, which is especially important for determining the emissivity profile near the plasma edge. The tomography result is also interesting, in so far as it shows how the two-camera measurement can be used for a successful reconstruction of the emissivity contours. This is true even for a case where the number of channels is relatively small, although the errors in the data must be negligible. When the latter is not true (as in Fig.20a), large edge oscillations can appear in the fitted brightness profile (Fig.20b) as well as in the emissivity profile (Fig.23). The Abel inversion is less affected by random noise, as can be seen in Fig.22, where deduced and original emissivity profiles are compared. It should be noted that the perturbed profile shown in Fig.20 is just one example of several tests we performed using different values for the perturbation of the data, but taking always a perturbation level (±20 maximum) reproducing the experimental uncertainties. All these tests gave similar results.

b) Broad Profiles

The neutron brightness profile of Fig.3b is representative for broad profiles observed in JET during high current Ohmic discharges. The Generalized Abel Inversion gives an emissivity which appears reasonable although it is very depressed in the centre (Fig.25). On the other hand, the result of the tomography method is hardly realistic because of the huge oscillations in the emissivity profile (Figs.24,26). The unperturbed artificial profile resembling the profile of Fig.3b used to test these results is flat in the centre and then falls off steeply at larger radii. The results of the inversions of this profile (Fig.27-30) show again that both methods give acceptable results when unperturbed data are used as input, with the Generalized Abel In-

version always appearing to be the more accurate one. When the profile is broad, however, the validity of the inversion is limited by the spatial range of the brightness measurements. In the case of the artificial broad profile with random noise, the Cormack Tomography (Fig.31,33) gives a result that seems not to be realistic. The result of the Generalized Abel Inversion, however, is still in fair agreement with the original emissivity profile (Fig.32). It should be noted, though, that the resulting profile is hollow in the centre, where the original profile is flat. This indicates that the uncertainties in the data can distort Abel inversion results considerably in the central part of the emissivity profile. In particular, one should be cautious before attributing a physical significance to hollow neutron emissivity profiles, since this could be entirely a consequence of experimental uncertainties.

One last result from tests with artificial data concerns an estimate of the uncertainties in the T_D profiles that can be deduced from the Abel inversion of neutron brightness data. This was done by comparing the deduced profiles with the original analytical T_D profiles, as shown in Fig.34 for the broad profile cases. In particular, the difference between deduced and original profile was used to estimate the uncertainty propagating to T_D (absolute value and profile shape) from random uncertainties in the input data. This estimate is used in the following section, where the different sources of uncertainty in the T_D profiles from Abel inversion of neutron brightness data are discussed.

6. Deuterium Temperature Profiles

The T_D profiles shown in Fig.35 and 36 were deduced from the Abel inverted neutron emissivity profiles of Fig.13 and 25, using Eq.2 and the ex-

perimental n_e profiles of Fig.6. The plasma density ratio n_D/n_e was determined from the chordal-average Z_{eff} value, as described in Sect.2. To reduce the absolute uncertainty of the emissivity profile (and hence of the T_D profile), the emissivity values were normalized to the total neutron yield measured with the fission chambers. This affects the absolute value of T_D, but has hardly any effect on the temperature profile, for instance, on the quantity $d\ln T_D/dR$ (Fig.35b and 36b).

The quantity is considered here since it can be used to derive the parameter $\eta_i = (d\ln T_D/dR)/(d\ln n_D/dR)$. The parameter η_i expresses the relative steepness of the T_D and n_D profiles and plays a fundamental role in the theory of the so-called ion-mixing and ubiquitous modes [21] which are fundamental to some theories on anomalous heat transport in toroidal plasmas (see for instance [22]). An experimental determination of this parameter is therefore of considerable interest, and here we present the first determination of η_i from analysis of neutron brightness data. In Fig.35b, we show the value of $\eta_i=3.8$ at one point of the plasma profile, while in Fig.37 we show the time evolution of the maximum value of η_i in the interval $3.4<R<3.6$ m during the same plasma discharge. Although the uncertainty in η_i is rather large (about ±40%), this experimental result should still be useful in the study of the energy transport properties of JET plasmas with peaked density profiles.

Since the determination of deuterium temperature profiles from neutron brightness measurements presented here is the first result of its kind, we discuss in some detail the errors affecting T_D and η_i. For the sake of illustration we assume here that the neutron emissivity, g, has an exponential dependence on T_D,

$$g \propto T_D^{\alpha} n_e^2 \nu^2 \qquad (16)$$

where all quantities are functions of the major radius R used as a profile coordinate, and ν is the density ratio n_D/n_e. Specifically, the exponent α is a function of T_D, i.e. $\alpha(T_D) = d\ln\langle\sigma v\rangle/d\ln T_D$ but this is rather weak with $\alpha \approx 3$ for T_D=5 keV. From Eq.16, the uncertainty in the value of T_D and $d\ln T_D/dR$ can be evaluated separately. For T_D,

$$\left(\frac{\Delta T_D}{T_D}\right)^2 = \left(\frac{1}{\alpha}\frac{\Delta g}{g}\right)^2 + \left(\frac{2}{\alpha}\frac{\Delta n_e}{n_e}\right)^2 + \left(\frac{2}{\alpha}\frac{\Delta \nu}{\nu}\right)^2 \qquad (17)$$

where $\Delta T_D/T_D$ is the relative probable error in T_D and similarly for the other quantities. The error in g has contributions from the absolute calibration of the total neutron emission (±15%), and from the instrumental relative uncertainties and the assumed emissivity contours (±30%); the latter value is somewhat arbitrary and can only be estimated based on experience from analysing JET results. The electron density has a rather small uncertainty (±10%), while the error in ν is estimated as follows. Assuming for simplicity that only one main impurity ion species of charge Z_I is present in the JET plasma (say Z_I=6) we have $\nu=(Z_I-Z_{eff})/(Z_I-1)$ and $\Delta\nu/\nu=\Delta Z_{eff}/(Z_I-Z_{eff})$; clearly, ν becomes less well determined the higher the value of Z_{eff}/Z_I. Taking ±20% as the experimental uncertainty in the measured chord averaged Z_{eff}, and ±30% as a typical relative variation of Z_{eff} around the average across the profile, it is found that the resulting error on T_D dominates the other sources of uncertainty for $Z_{eff}/Z_I \geq 1/3$. More precisely, when all uncertainty contributions are added quadratically, the

probable uncertainty in T_D resulting from Eq.17 is ±13% for Z_{eff}=1 (pure deuterium), while it is ±27% for Z_{eff}=3 and Z_I=6. This strong dependence of the uncertainty in T_D on Z_{eff} represents a considerable limitation of the applicability of this method for the determination of T_D to JET plasmas, where usually $Z_{eff} \geq 3$.

The uncertainty in the value of $d\ln T_D/dR$ can be derived from

$$\frac{d\ln T_D}{dR} = \frac{1}{\alpha}\frac{d\ln g}{dR} + \frac{2}{\alpha}\frac{d\ln n_e}{dR} + \frac{2}{\alpha}\frac{d\ln \nu}{dR} \qquad (18)$$

which is obtained upon differentiation of Eq.16. We can attribute a value of ±0.4 m^{-1} to the error in $(1/\alpha)d\ln g/dR$, based on the results of the tests discussed in Sect.5 and on our experience in analysing the data. The error in $d\ln n_e/dR$ should be about ±0.3 m^{-1}, which again is an estimate based mainly on experience in analysing density measurement data. As for the quantity $d\ln\nu/dR$, this has tacitly been assumed to be zero, and any deviation from zero is included as an uncertainty of the method. A simple estimate gives $(2/\alpha)d\ln\nu/dR \leq 0.3$ m^{-1} for $Z_{eff} \leq 3$. Summing up quadratically all contributions we obtain a value of ±0.6 m^{-1} for the error on $d\ln T_D/dR$.

Finally, the error in η_i is determined by adding quadratically the errors in $d\ln T_D/dR$ and $d\ln n_D/dR$. The error in $d\ln n_D/dR$ is the dominant contribution to the resulting ±40% uncertainty; this shows that the determination of the T_D profile presented in this paper is relatively accurate for this kind of studies.

7. Discussion

Taking the magnetic flux surfaces as emissivity contours constitutes a source of uncertainty both in the radial position of the contours (although

correctable as mentioned above) and in the vertical elongation of the contours. These uncertainties can be significant especially near the plasma center as shown in a recent work by R.S.Granetz et al. [23] based on soft X-ray measurements. These can provide a more direct information of the two-dimensional current distribution near the magnetic axis than the magnetic field measurements external to the plasma. For this reason the topology of the soft X-ray emissivity was used in Ref.[6] for analysing the polarimetric measurements of the poloidal field distribution in JET plasmas. In this case, the plasma safety factor at the magnetic axis, q_0, was the main aim of the analysis. Since q_0 is proportional to the square of the central flux surface elongation, its determination is very sensitive to uncertainties in the central geometry. In our case, an error in the elongation can affect the projection of the brightness data from the horizontal camera. However, its effect is reduced when the data from both cameras are combined, so our analysis should not be very sensitive to changes in the central elongation.

Errors in the central elongation can also affect the volume integrated emissivity (i.e., the total neutron yield), especially if the emissivity profile is very peaked. This could in part explain the large difference (over 50% for the data of Fig.3a) between the volume integrated emissivity and the total neutrn yield determined by fission chamber measurements: a difference of about 20% is usually observed, probably due to uncertainties in the absolute calibration of the detectors of the neutron cameras. Note that the emissivity profiles were reduced by 20% in absolute value (assumed normalization factor) before deducing the T_D profiles of Fig.35-36. The larger difference observed for the profile of Fig.3a can be explained by an overestimation of the central elongation either due to a mis-identification of the equilibrium in this case, or to real differences between the emissivity topology and the

magnetic flux surfaces. In this work we have not pursued the investigation of this discrepancy, since attempts to improve the assumed emissivity topology would not be very useful for the present kind of analysis.

The sensitivity of the Cormack Tomography to random errors in the experimental data is partly due to using a polynomial fit to the data. We believe that other tomography methods (intermediate between the Cormack Tomography and the Generalized Abel Inversion) could give better results. For instance one could use the Constrained Tomography method described in Ref.[3], which performs a piecewise interpolation of the brightness data instead of a polynomial fit. In this case the inversion of the outer brightness profile is not affected by the errors in the central chords, which is an advantage over the Cormack Tomography. However, we do not see any overall advantage of this inversion method over the Generalized Abel Inversion for the cases considered here, since the emissivity contours determined with this tomography method are considerably prone to be distorted by the uncertainties of the brightness data. The only cases where the Constrained Tomography of the neutron brightness data could be of interest are the plasmas where the emissivity contours depart from the magnetic flux surfaces. This is the case for plasma discharges with additional deuterium beam heating, resulting in a significant fraction of beam ions being trapped. In these cases an outward radial displacement of the emissivity contours should occur.

A special limitation of the analysis presented here has already been pointed out, namely the requirement that the average Z_{eff} must be small (≤ 3). In fact, this is one of the main limitations in the present plasmas of the JET machine, and considerable effort is being put into the study of this problem. An improvement in the plasma purity has been obtained by in-

creasing the plasma density by pellet fuelling, and more recently by using beryllium limiters. In any case, the method presented here to determine the T_D profiles can only have a limited use for JET plasmas since it cannot directly be applied to beam heated plasmas. However, the examples presented here can be regarded as a demonstration of the diagnostic principle, in view of future applications of this T_D diagnostic technique in planned machines like Ignitor [24] and CIT [25], which will have denser and, hopefully, cleaner plasmas and will not rely on additional beam heating.

Finally, we make some comments on the results on $T_D(R)$ deduced from neutron brightness profiles. Since other temperature measurements are available in JET plasmas, we compare data from these measurements with the T_D profiles deduced in this work. In Fig.38, the T_D profile of Fig.35 is plotted along with the T_e profile determined from ECE measurements [26]. Besides the errors in the absolute value of the two temperatures, both results are subject to uncertainties in the radial position of the data points. In the case of the T_D profile, these uncertainties are due to the assumed emissivity contours (corrected in the way described in Sect.4), while for the T_e profile the uncertainty comes from the paramagnetic corrections to the vacuum toroidal field used in the analysis of the ECE data. As a result, a relative displacement of the T_D and T_e profile peaks can be observed, while both profiles show an additional outward shift relative to the magnetic axis position for the identified plasma equilibrium. The comparison of the two temperature profiles shows another interesting feature, namely the rapid change of the temperature gradient occurring at R≈3.6m, which is present in both profiles (and also in the n_e profile, see Fig.6). This feature, indicating a change in the electron and ion thermal conductivities along the profile, is also observed in the carbon temperature profile of Fig.39. This profile

was measured by active charge exchange spectroscopy [27] in a plasma discharge similar to the one in Fig.4a, apart from the presence of 5 MW of additional deuterium beam heating injected into the plasma for diagnostic purposes. The two ion temperature measurements appear to give overall similar results, apart from the uncertainties in the radial position of the profile points. In the latter example, the T_e profile from LIDAR Thompson scattering measurements [17] is also available; the outward shift of this profile is less pronounced compared to the T_e profile from ECE, showing that this shift is partly due to experimental uncertainties.

In Fig.40 we show the time evolution of the peak ion temperature during the JET plasma discharge of Fig.4a, as determined in the present analysis and as obtained from the X-ray crystal spectrometer measurements [28]. The agreement is very good. This result indicates that the velocity distribution of the plasma deuterium is Maxwellian, even in the presence of substantial ICRF heating of plasma minority ions.

Also the T_D profile of Fig.36 can be compared with other temperature profiles, and in particular with the T_D profile determined by the Neutral Particle Analyser array [29]. This comparison is shown in Fig.41. Again the agreement of the two profiles is within the uncertainties in the radial position and absolute value of the profile data points. It should be noted that the shapes of the T_D and T_e profiles are similar in the examples shown here, supporting the assumption made in Ref.[9].

8. Conclusions

A detailed analysis of the JET neutron brightness data has been carried out. We find that the two-dimensional features of the neutron emissivity cannot generally be determined with sufficient accuracy from the present

brightness data. The main cause for this limitation is attributed to the uncertainties of the experimental brightness data. In cases where the neutron emissivity contours are known from other measurements (such as the external magnetic measurements providing an identification of the magnetic flux surfaces) the Generalized Abel Inversion of the neutron brightness data allowed a fairly accurate determination of the radial emissivity profiles. These profiles, together with the experimental electron density profiles and the average Z_{eff} values, were used to deduce the deuterium temperature profiles in plasmas with Maxwellian deuterium velocity distributions. Results of application of this method for analysing neutron brightness profiles have been presented here using representative JET data as an example. These results were compared to other ion temperature measurements in terms of accuracy and space resolution and agreement was obtained. In general, the accuracy of the results depends crucially on the plasma purity so that the neutron method is applicable only in cases where Z_{eff} is small (typically $Z_{eff} \leq 3$). We conclude that the Generalized Abel Inversion of the neutron brightness data can be used for the diagnosis of JET plasmas, but with limited applicability as to types of plasma conditions. On the basis of present experience we would anticipate that neutron emissivity measurements would play an important role for the diagnosis of high density plasmas approaching ignition like in Ignitor and CIT.

Acknowledgements

The authors are grateful to Dr.J.M.Adams and N.Watkins for kindly providing the examples of neutron brightness data analysed in this paper, and to Dr.O.N.Jarvis and Dr.G.Sadler for discussions concerning the data. Dr.R.S.Granetz is gratefully acknowledged for providing the computer code

used for the Cormack Tomography, as well as for useful comments on the results of this work. Dr.E.Lazzaro, B.Keegan and A.Galway are also acknowledged for their help in providing the magnetic flux surfaces from the equilibrium identification code IDENTC. The authors are grateful to Dr.P.Smeulders for pointing out the interest of the use of the Constrained Tomography method for the analysis of neutron brightness data. One of the authors (G.G.) is also grateful to Dr.J.Kallne, Dr.F.Pegoraro and Dr.A.Taroni for their support throughout the development of this work. Finally the authors wish to thank the JET Experimental Department for the other experimental measurements used in this work.

References

[1] Kallne,J., The Role of Neutron Measurements in the Study of Burning Fusion Plasmas, Rep. PTP 88/16, Massachussets Institute of Technology, Cambridge, Massachusetts (1988), submitted for publication in Comments Plasma Phys. Control. Fusion, and Kallne,J., Neutron Measurements in the Study of Fusion Plasma Physics with Tokamaks, Rep. PTP 88/11, Massachussets Institute of Technology, Cambridge, Massachusetts (1988).

[2] Adams,J.M., Jarvis,O.N., Kallne,J., et al., in Controlled Fusion and Plasma Physics (Proc. 14th Eur. Conf. Madrid, 1987), Vol. 11D, Part III, European Physical Society (1987)1224, and Adams,J.M., Cheetham,A., Conroy,S., et al., in Controlled Fusion and Plasma Physics (Proc. 16th Eur. Conf. Venice, 1989), Vol. 13B, Part I, European Physical Society (1989), 63.

[3] Granetz,R.S., Smeulders,P., Nucl.Fusion 28 (1988)457.

[4] Gottardi,N., Krause,H., Mast,K.F., in Controlled Fusion and Plasma Physics (Proc. 12th Eur. Conf. Budapest, 1985), Vol. 9F, Part I, European Physical Society (1985)30.

[5] Bartlett,D.V., Campbell,D.J., Costley,A.E., et al., in Controlled Fusion and Plasma Heating (Proc. 15th Eur. Conf. Dubrovnik, 1988), Vol. 12B, Part III, European Physical Society (1988)1119.

[6] O'Rourke,J., Blum,J., Cordey,J.G., et al., in Controlled Fusion and Plasma Heating (Proc. 15th Eur. Conf. Dubrovnik, 1988), Vol. 12B, Part I, European Physical Society (1988)155.

[7] Morgan,P.D., O'Rourke,J., in Controlled Fusion and Plasma Physics (Proc. 14th Eur. Conf. Madrid, 1987), Vol. 11D, Part III, European Physical Society (1987)1240, and Morgan,P.D., in Controlled Fusion and Plasma

Heating (Proc. 15th Eur. Conf. Dubrovnik, 1988), Vol. 12B, Part I, European Physical Society (1988)139.

[8] Peres,A., J.Appl.Phys. 50(1979)569.

[9] Jarvis,O.N., Gorini,G., Kallne,J., et al., Nucl.Fusion 27 (1987)1755.

[10] Gorini,G., Hone,M., Jarvis,O.N., et al., in Basic Physical Processes of Toroidal Fusion Plasmas (Proc. Workshop Varenna, 1985), Vol.2, CEC, Brussels (1986)699.

[11] Elevant,T., Olsson,M., Grosshoeg,G., in Bull. Am. Phys. Soc., Vol.32, San Diego (1987) 1870.

[12] Knoll, G.F., Radiation Detection and Measurement, J. Wiley and Sons (1979)585.

[13] Verschuur,K., and Jarvis,O.N., private communication.

[14] Jarvis.O.N., Kallne,J., Sadler,G., van Belle,P., Merlo,V., Further Calibration of the Time Resolved Neutron Yield Monitor, Rep. JET-IR(85)06, JET Joint Undertaking, Abingdon, Oxfordshire (1985).

[15] Blum,J., Gilbert,J.C., Le Foll,J.L., Thoorin,B., in Proc. 8th Eur. Conf. on Comput. Phys, Vol 10D, Eibsee (1986)49.

[16] Lazzaro,E., Mantica,P., Plasma Phys. Contr. Fus. 30(1988)1735.

[17] Salzmann,H., Hirsch,K., Nielsen,P., et al., Nucl.Fusion 27 (1987)1925.

[18] Veron,D., in Diagnostics for Fusion Reactor Conditions (Proc. Workshop Varenna, 1982), Vol.2, CEC, Brussels (1983)283.

[19] Behringer,K., Denne,B., Edwards,A., et al., in Controlled Fusion and Plasma Heating (Proc. 15th Eur. Conf. Dubrovnik, 1988), Vol. 12B, Part I, European Physical Society (1988)338.

[20] Cormack,A.M., J. Appl. Phys 9(1963)2722, and Cormack,A.M., J. Appl. Phys 10(1964)2908.

[21] Coppi,B., Pegoraro,F., Nucl.Fusion 17(1977)5.

[22] Romanelli,F., Briguglio,S., Toroidal Semicollisional Microinstabilities and Anomalous Electron and Ion Transport, Rep.JET-P(88)31, JET Joint Undertaking, Abingdon, Oxfordshire (1988), submitted for publication in Physics of Fluids.

[23] Christiansen,J.P., Callen,J.D., Ellis,J.J., Granetz,R.S., Determination of Current Distribution in JET from Soft X-ray Measurements, submitted for publication in Nuc.Fusion, and Granetz,R.S., personal communication (1988).

[24] Coppi,B., Comments Plasma Phys. Control. Fusion 3(1977)2, and Coppi,B., Lanzavecchia,L., Ibid 11(1987)47.

[25] Schmidt,J., et al., in Plasma Physics and Nuclear Fusion Research (Proc. 11th IAEA Conf., Kyoto, 1986), Vol.III, IAEA (1986) 259.

[26] Bartlett,D.V., Campbell,D.J., Costley,A.E., et al., in Controlled Fusion and Plasma Physics (Proc. 14th Eur. Conf. Madrid, 1987), Vol. 11D, Part III, European Physical Society (1987)1252.

[27] von Hellermann,M., Boileau,A., Horton,L., et al., in Controlled Fusion and Plasma Heating (Proc. 16th Eur. Conf. Venice, 1989), Vol. 13B, Part I, European Physical Society (1989)107.

[28] Bartiromo,R., Bombarda,F., Giannella,R., et al., The JET High Resolution Bent Crystal Spectrometer, Rep.JET-P(88)11, JET Joint Undertaking, Abingdon, Oxfordshire (1988), Rev. Sci. Instrum. 60 (1989) 237, and Bombarda,F., Giannella,R., Kallne,E., et al., Ion Temperature Measurements from Doppler Broadening of He-like Nickel Lines, accepted for publication in J. Quant. Spectrosc. Radiat. Transfer.

[29] Bracco,G., Corti,S., Zanza,V., et al., First Results from JET Neutral Particle Analyser (NPA), Rep.JET-IR(84)04, JET Joint Undertaking,

Abingdon, Oxfordshire (1984), and Corti,S., Barbato,E., Bracco,G., et al., in Controlled Fusion and Plasma Physics (Proc. 13th Eur. Conf. Schliersee, 1986), Vol. 10C, Part I, European Physical Society (1986)109.

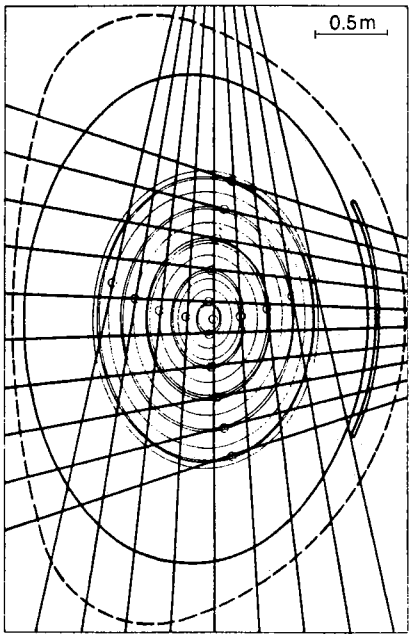

Fig. 1

1. Lines of sight of the neutron brightness measurements at JET. The cross section of the magnetic flux surfaces tangential to each line are also shown for JET discharge 13979 at t=52.0 s. The points of tangency are marked with a circle.

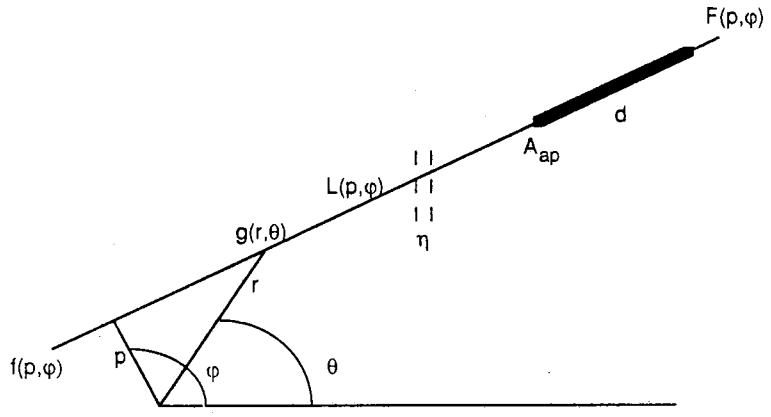

Fig. 2

2. Schematics of the collimation geometry for a single channel of the multicollimator. (r,θ) are polar coordinates on the plasma cross section, while p is the radius and φ is the angle of the viewing line $L(p,\varphi)$. $g(r,\theta)$ is the neutron emissivity and $f(p,\varphi)$ is its line-integral (brightness) over $L(p,\varphi)$. The measured neutron flux at the detector, $F(p,\varphi)$, is collected through a collimator of length d and aperture area A_{ap}; η is an attenuation factor (taking into account the presence of vacuum windows etc. along the line of sight).

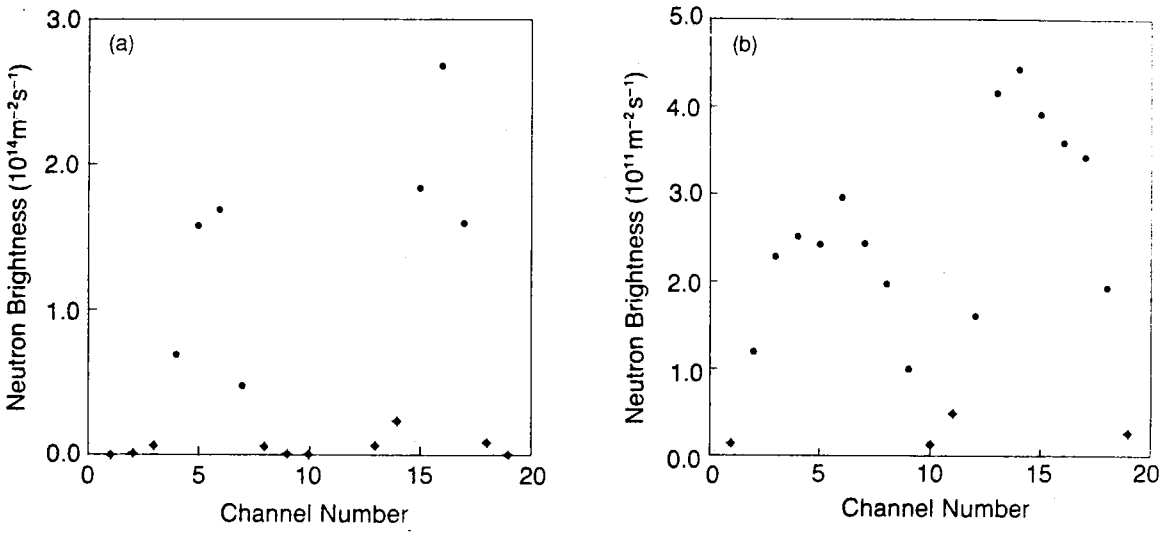

Fig. 3

3. a) Neutron brightness profile for JET discharge 16211 during the time interval t=44.2 to 44.3 s, plotted vs channel number. Channels 1-10 belong to the horizontal camera, and channels 11-19 belong to the vertical camera. The data have been reduced so that they represent the brightness values as would be measured along collimation lines of small poloidal width. This required a small correction to the data points marked with a cross. For this particular example, channels 11 and 12 (not shown here) were dominated by background.

b) Neutron brightness profile for JET discharge 13979 during the time interval t=48.0 to 55.0 s, plotted vs channel number. The data points marked with a cross were corrected for the reason explained in a).

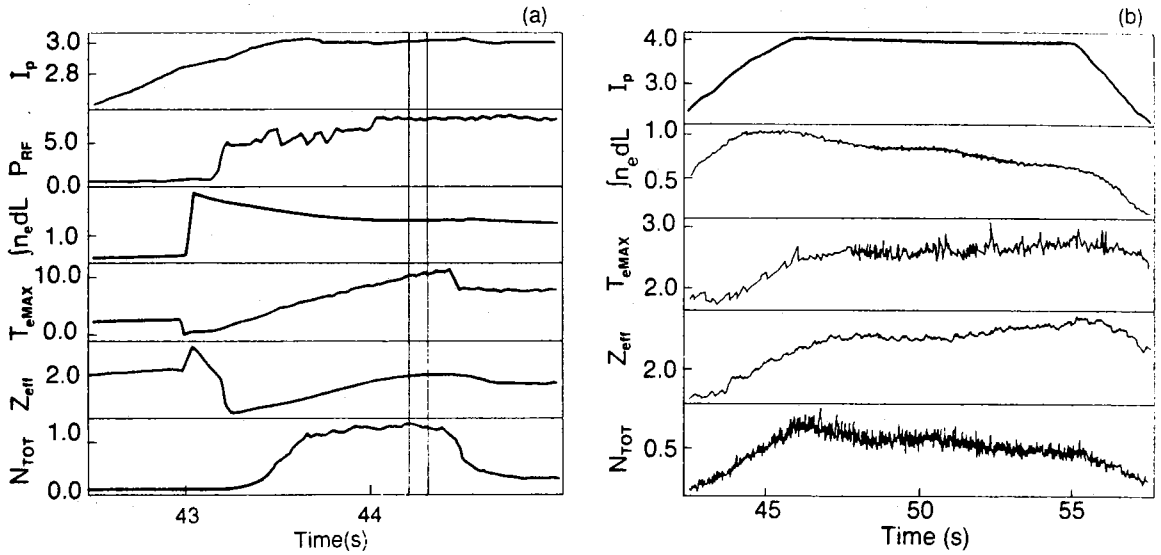

Fig. 4

4. a) Plasma current (I_p, MA), ICRF heating power (P_{RF}, MW), chord averaged density ($\int n_e dL$, 10^{20} m^{-2}), maximum electron temperature (T_{eMAX}, keV), chord-averaged effective ion charge (Z_{eff}) and total neutron emission (N_{TOT}, 10^{15} s^{-1}) for JET discharge 16211. The discharge starts at 40.0 s. The time interval corresponding to the neutron brightness measurement of Fig.3a is also indicated.

b) Plasma current (I_p, MA), chord averaged density ($\int n_e dL$, 10^{20} m^{-2}), maximum electron temperature (T_{eMAX}, keV), chord-averaged effective ion charge (Z_{eff}) and total neutron emission (N_{TOT}, 10^{13} s^{-1}) for JET discharge 13979. The time interval corresponding to the neutron brightness measurement covers the entire current flat top.

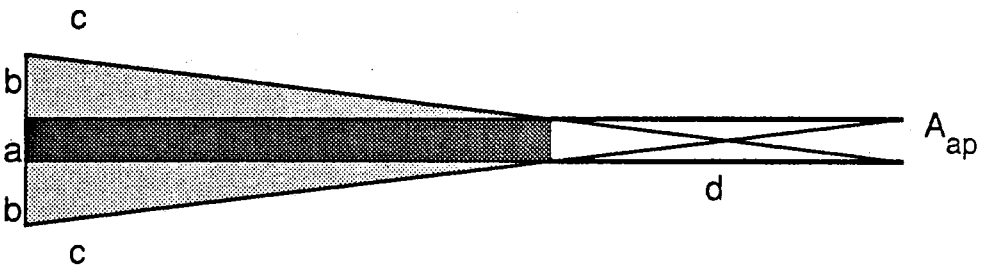

Fig. 5

5. Collimation geometry model used in the data reduction. Neutrons emitted from the region a are seen by the entire detector surface, those emitted from b are seen by a fraction of the detector, and those emitted from c are not seen. As a result, the neutron flux at the detector is representative of an average brightness over the area a+b.

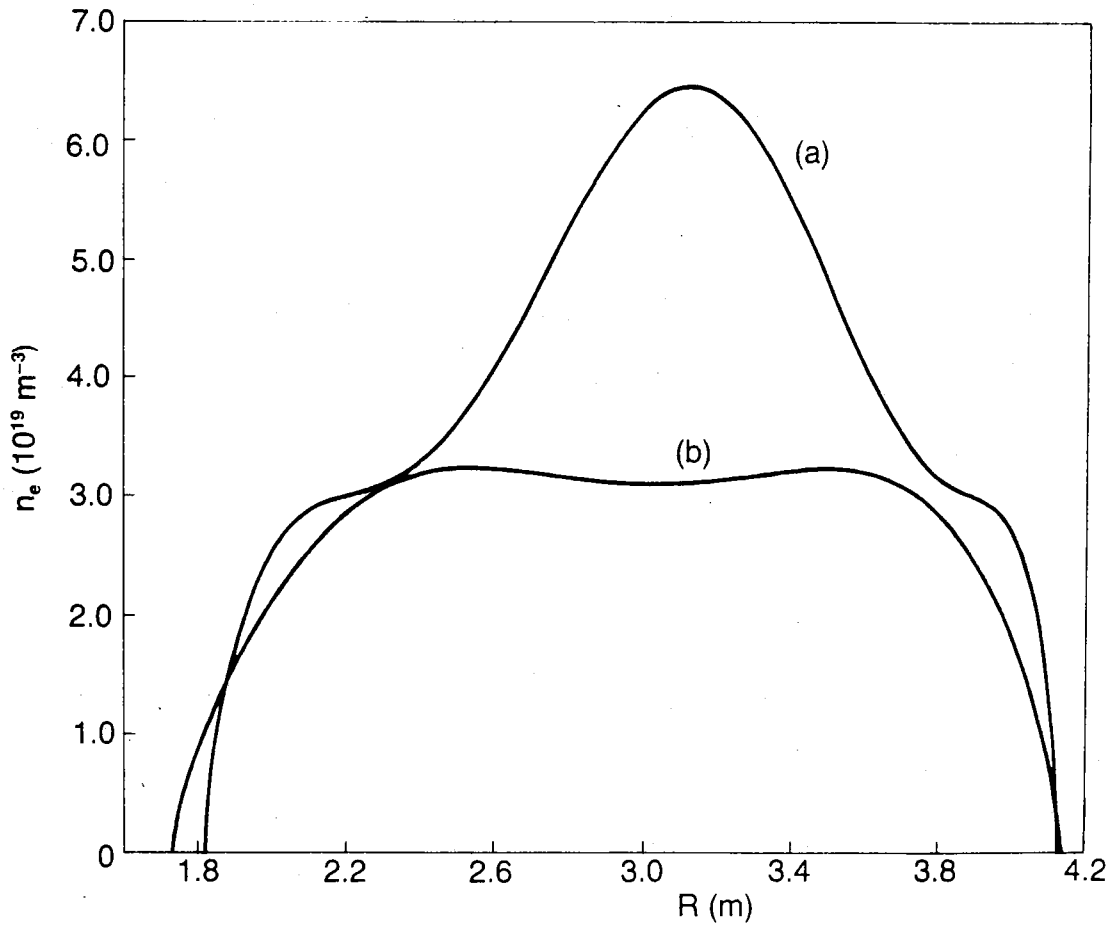

Fig. 6

6. Electron density profiles from Generalized Abel Inversion of Interferometric measurements of the chord-integrated density for JET discharge 16211 at time t=44.24 s (a), and for JET discharge 13979 at time t=52.0 s (b).

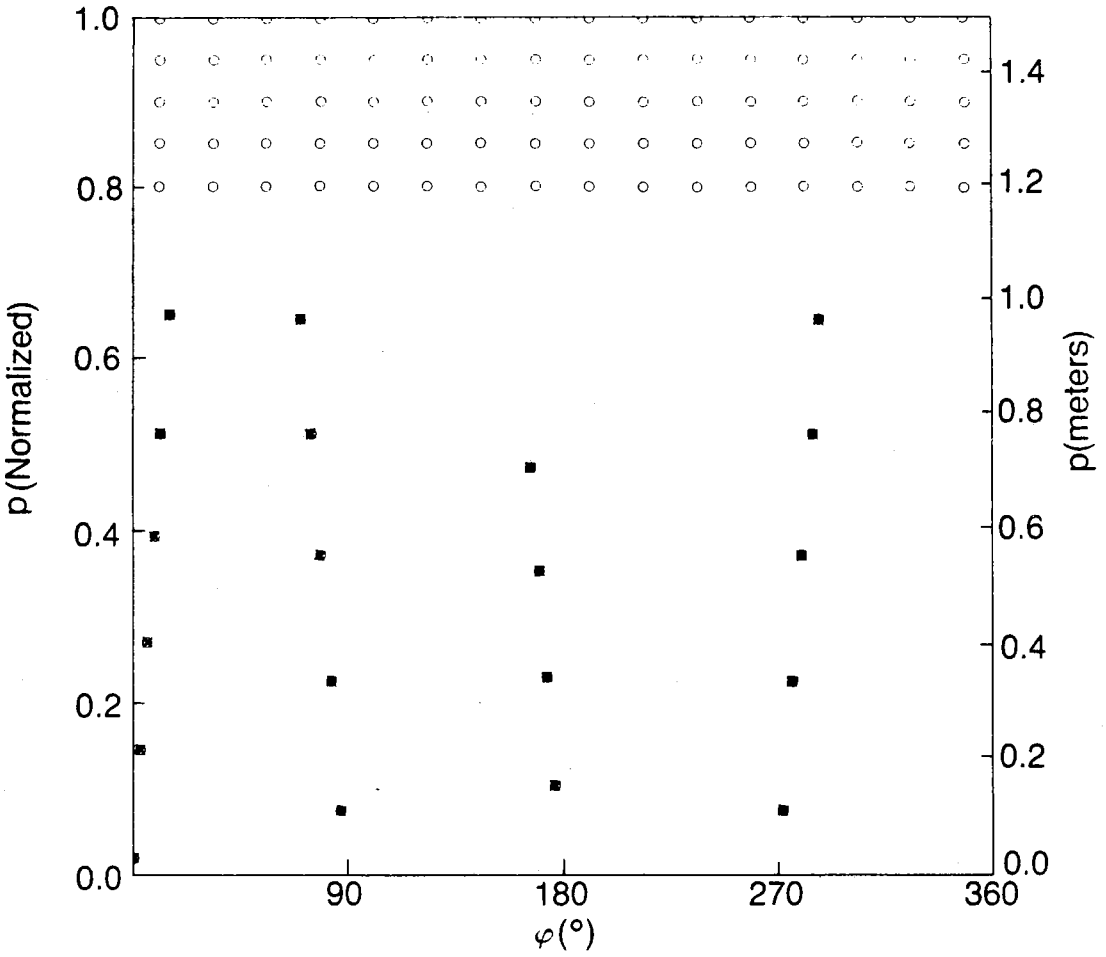

Fig. 7

7. Location of the viewing chords in the (p,φ) plane. In this example, the centre of the coordinate system is at R=3.03 m, z=0, corresponding to the position of the magnetic axis for the magnetic topology of Fig.1. The radius of the circle delimiting the emitting region is set at 1.5 m. The 19 experimental chords (circled x's) lie on 4 approximately vertical lines on this plane, so they effectively sample the brightness at 4 values of φ. The open circles represent additional viewing chords of zero brightness added near the edge of the emitting region.

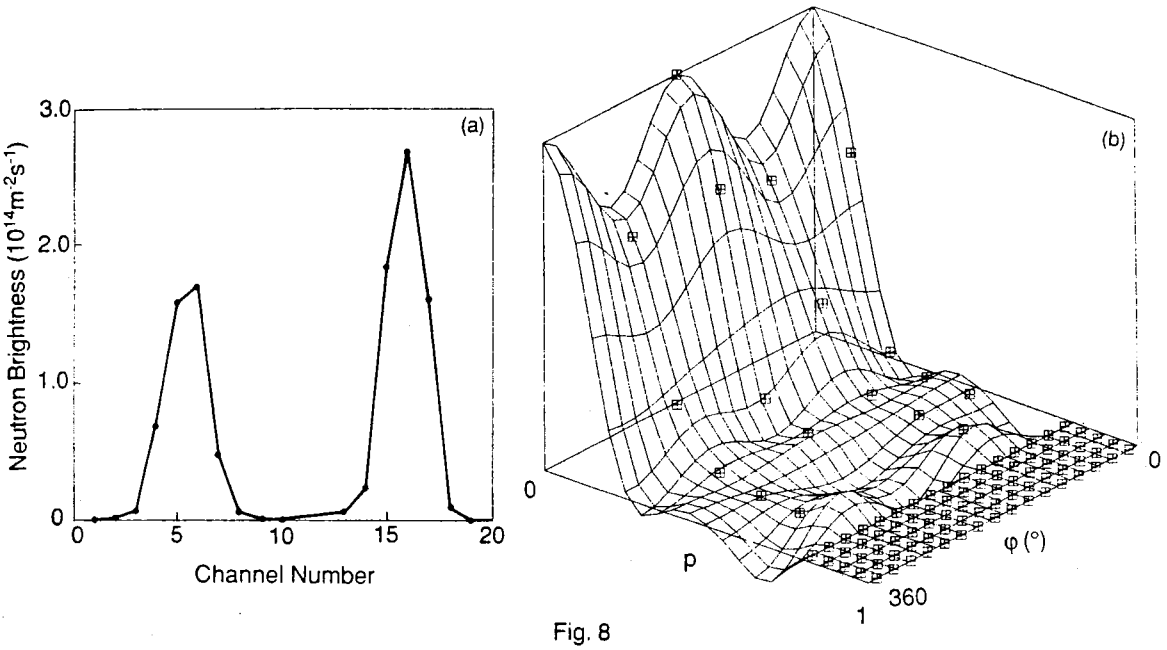

Fig. 8

8. Least-square fit to the experimental brightness profile of Fig.3a using the Cormack Tomography method.

a) Fit of the data vs channel number.

b) Same fit in the 2-dimensional (p,φ) space.

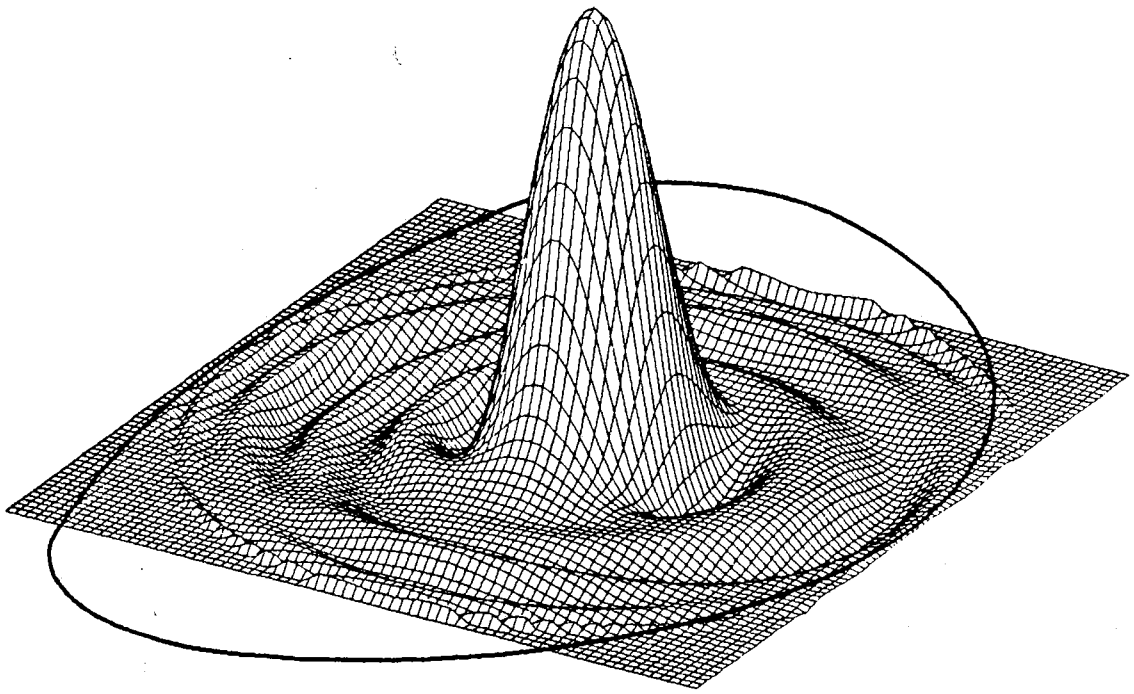

Fig. 9

9. Hidden line perspective plot of the neutron emissivity profile obtained by Cormack Tomography of the experimental brightness profile of Fig.3a. The maximum emissivity is $4.5 \cdot 10^{14}$ $m^{-3}s^{-1}$.

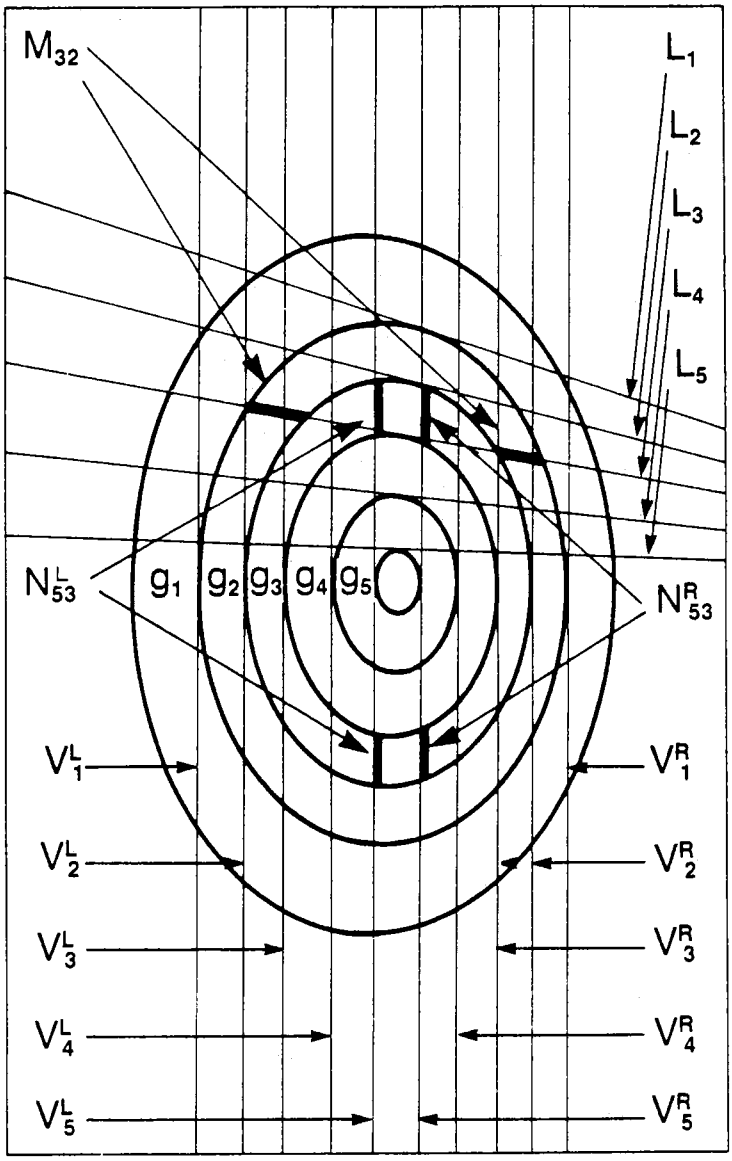

Fig. 10

10. Geometry for the projection of the brightness data (first step of the Generalized Abel Inversion) for a simplified system consisting of 5 channels. L_1-L_5 represent the experimental lines of sight, tangents to a set of magnetic flux surfaces. For the projection, the area within two such adjacent surfaces is taken as resolution element, or pixel. V^R_1- V^R_5 and V^L_1-$V^L_5$are two sets of vertical lines of sight tangential to the same set of pixels. The virtual brightnesses along these vertical lines are related linearly to the brightness values along the experimental lines (Eq.13-15). This linear relationship can be expressed in terms of the chordal lengths of the lines of sight within each pixel, and M_{32}, N^R_{53}, N^L_{53} are examples of such chordal lengths.

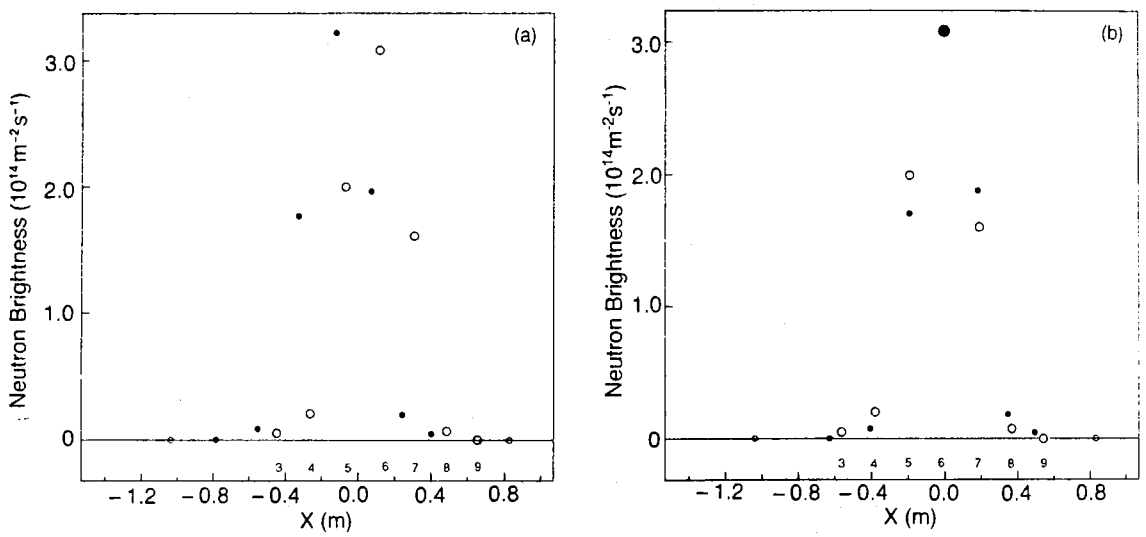

Fig. 11

11. Virtual brightness profile for the vertical neutron camera obtained from the experimental profile of Fig.3a. The distance from the emissivity axis is used here as X coordinate. The small circles on the line of zero emissivity indicate the assumed limits of the emitting region. For the projected brightness values an open symbol is used if the virtual and original lines of sight lie on the same side of the emissivity axis; otherwise a full symbol is used. For the open symbols, the corresponding channel numbers (here ranging from 3 to 9 for the vertical camera) are also indicated below the line of zero emissivity. Channels 1 and 2 of the vertical camera are not shown here because they were dominated by background. The open symbol profile is clearly shifted relative to the full symbol profile in a), where the magnetic flux surfaces are assumed as emissivity contours for the projection. This shift is removed in b) by moving the same contours radially outward by 12 cm. This example shows how a global position correction is generally sufficient for obtaining consistency between the brightness measurements and the magnetic topology.

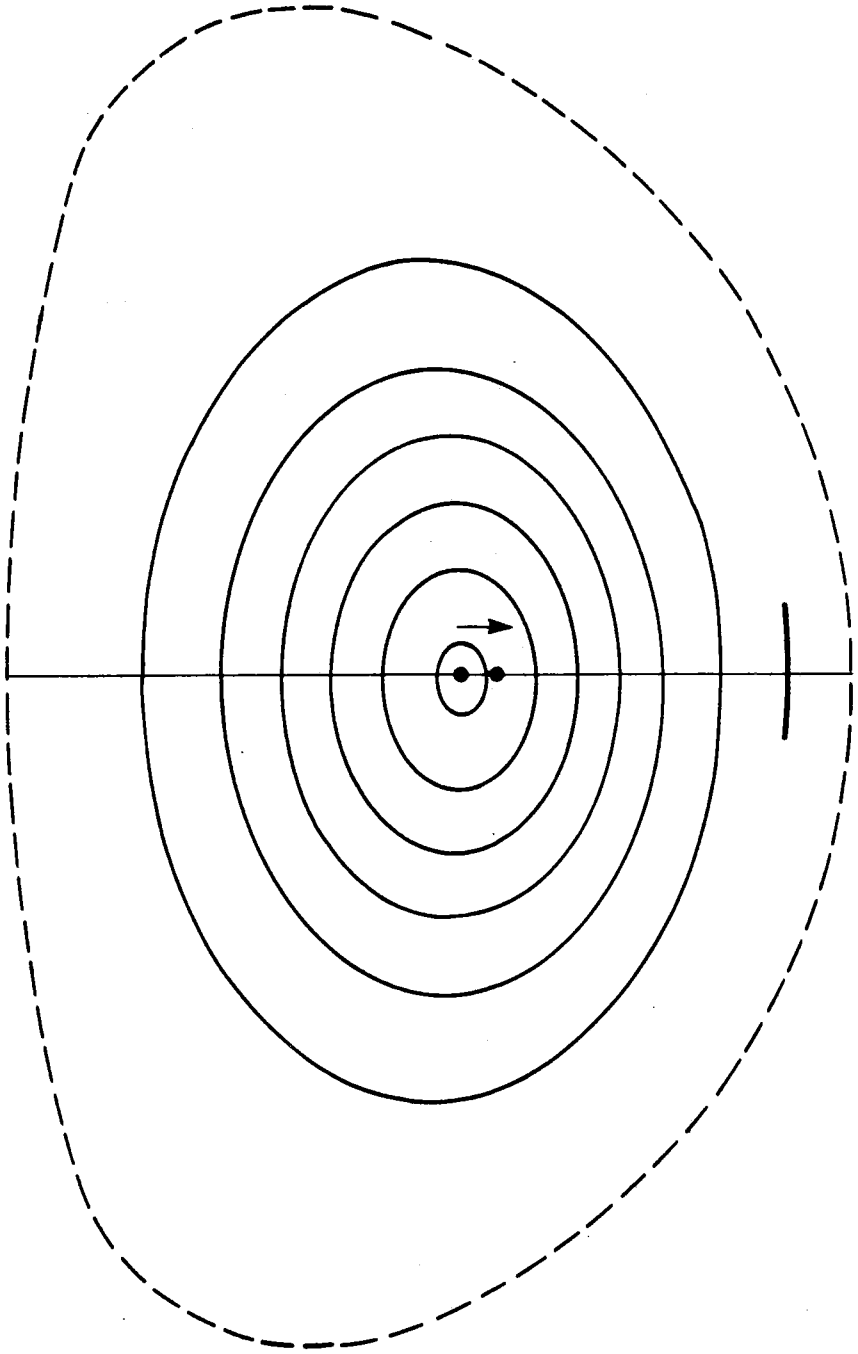

Fig. 12

12. Position of the emissivity axis (full circles) before and after the radial shift of Fig.11. This shift represents about 10% of the distance between the axis and the limiter (thick line). For comparison the vacuum vessel (dashed line) and the magnetic flux surfaces tangent to channels 1-5 of the horizontal camera are shown.

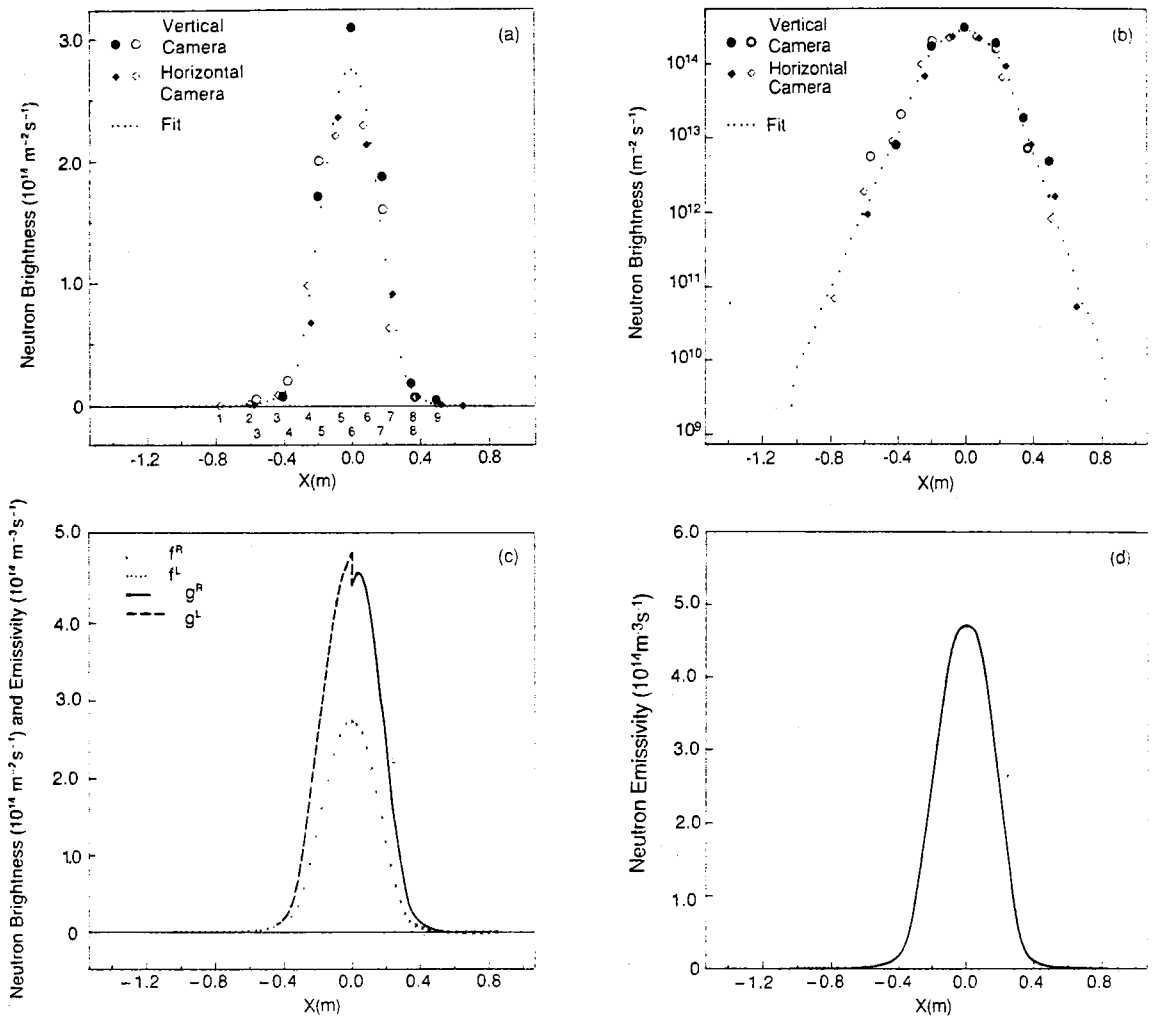

Fig. 13

13. Generalized Abel Inversion of the neutron brightness profile of Fig.3a.

a) Polynomial fit of the projected brightness data from both cameras. A few channels dominated by background were omitted from this analysis.

b) Same as a) but using a log scale for the y-axis. Near the edge of the emitting region the data are interpolated linearly.

c) Fitted brightness profiles (f^R and f^L) and corresponding emissivity profiles (g^R and g^L).

d) Neutron emissivity profile obtained by averaging g^R and g^L.

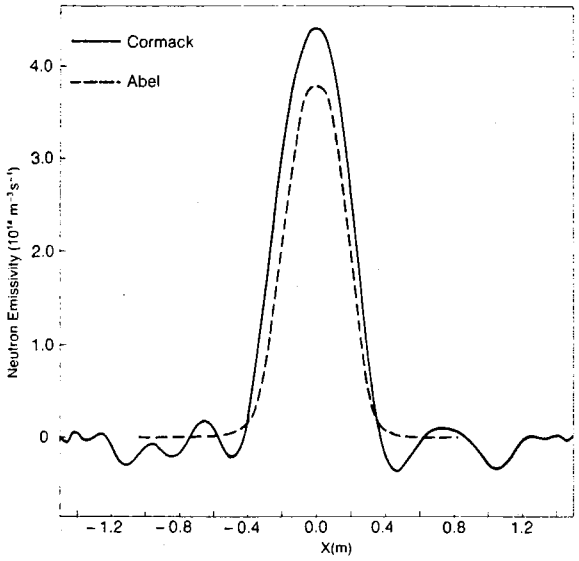

Fig. 14

14. Neutron emissivity profiles on the plasma equatorial plane as determined by Cormack Tomography (full line) and by Generalized Abel Inversion (dashed line) of the brightness profile of Fig.3a.

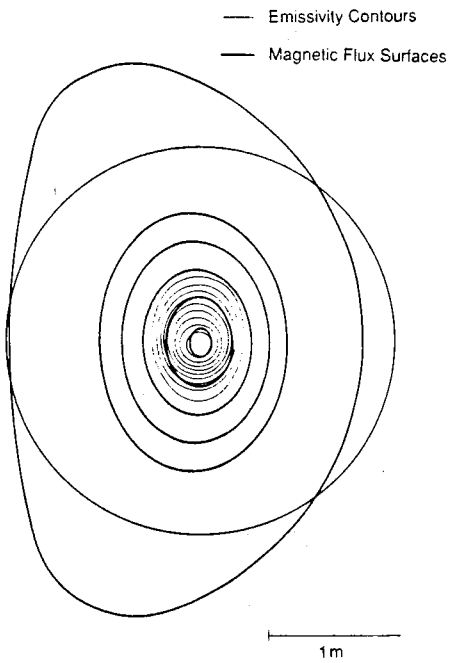

Fig. 15

15. Emissivity topology as determined by Cormack Tomography of the brightness profile of Fig.3a. The contours shown are at 10%, 20%, ..., 90% of the peak emissivity. Also shown are the vacuum vessel contours, the circle delimiting the emitting region and the magnetic flux surfaces tangent to channels 1-5 of the horizontal camera. The departure of the emissivity contours from the magnetic flux surfaces is significant.

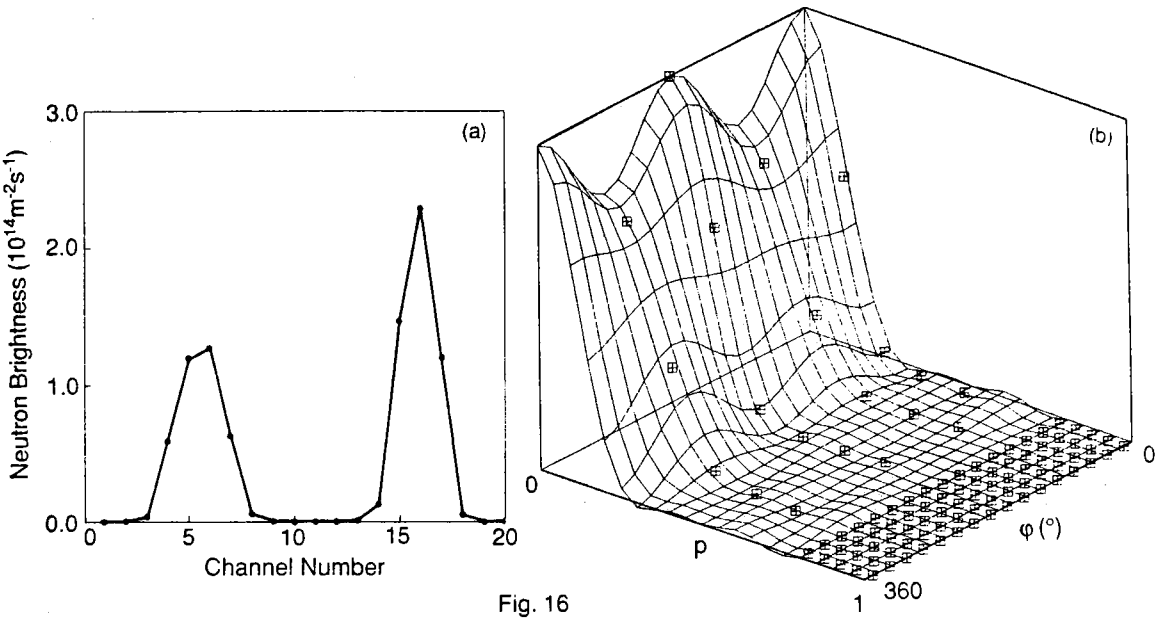

Fig. 16

16. Least-square fit to the first peaked artificial brightness profile using the Cormack Tomography method.

a) Artificial data vs channel number and fit.

b) Same fit in the 2-dimensional (p,φ) space.

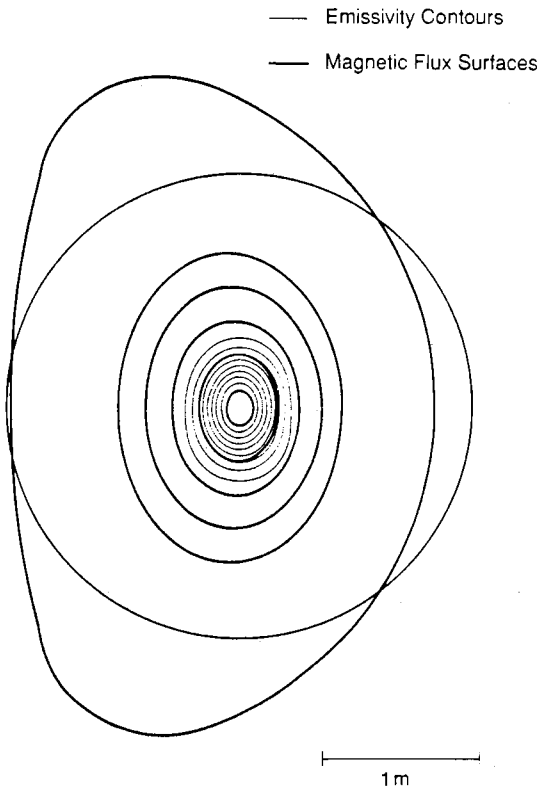

Fig. 17

17. Emissivity topology as determined by Cormack Tomography of the first peaked artificial brightness profile. The agreement between the tomography result and the original topology (magnetic flux surfaces) is good.

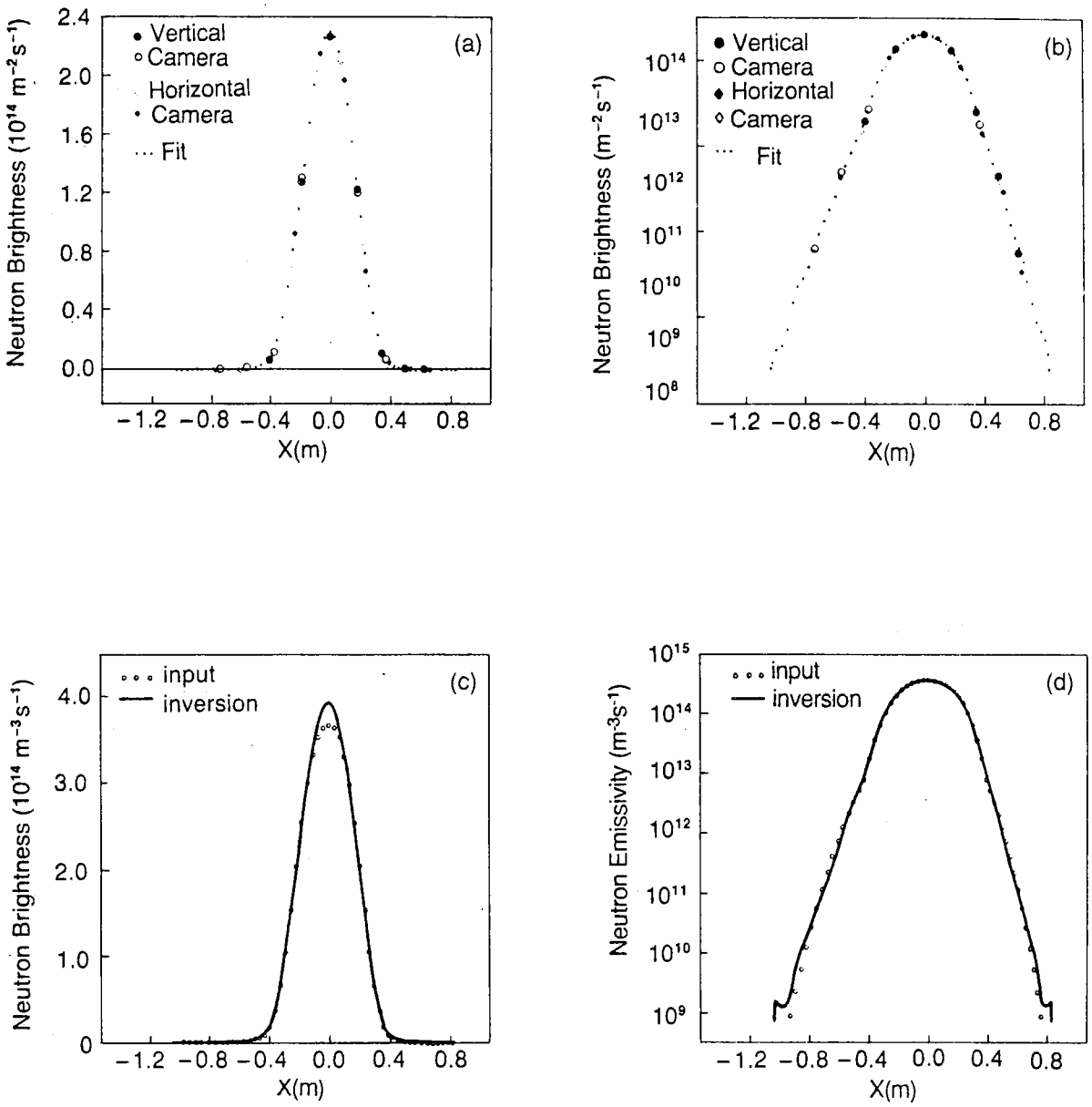

Fig. 18

18. Generalized Abel Inversion of the first peaked artificial profile.

a) Fit of the projected brightness data.

b) Same as a) but using a log scale for the y-axis.

c) Deduced emissivity profile and original profile (linear scale).

d) Deduced emissivity profile and original profile (log scale). The original emissivity profile is well reproduced over 4 orders of magnitude.

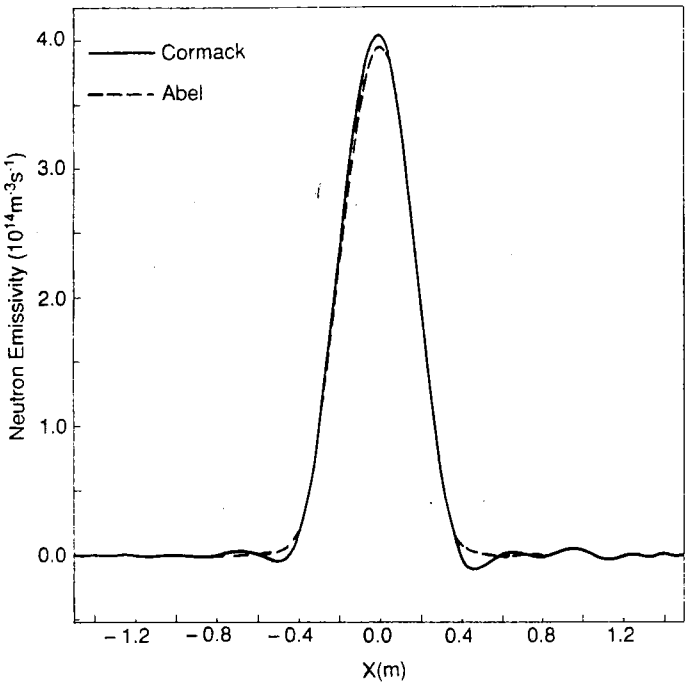

Fig. 19

19. Neutron emissivity profiles on the plasma equatorial plane as determined by Cormack Tomography (full line) and by Generalized Abel Inversion (dashed line) of the first peaked artificial profile. The agreement between the two profiles is good over two orders of magnitude.

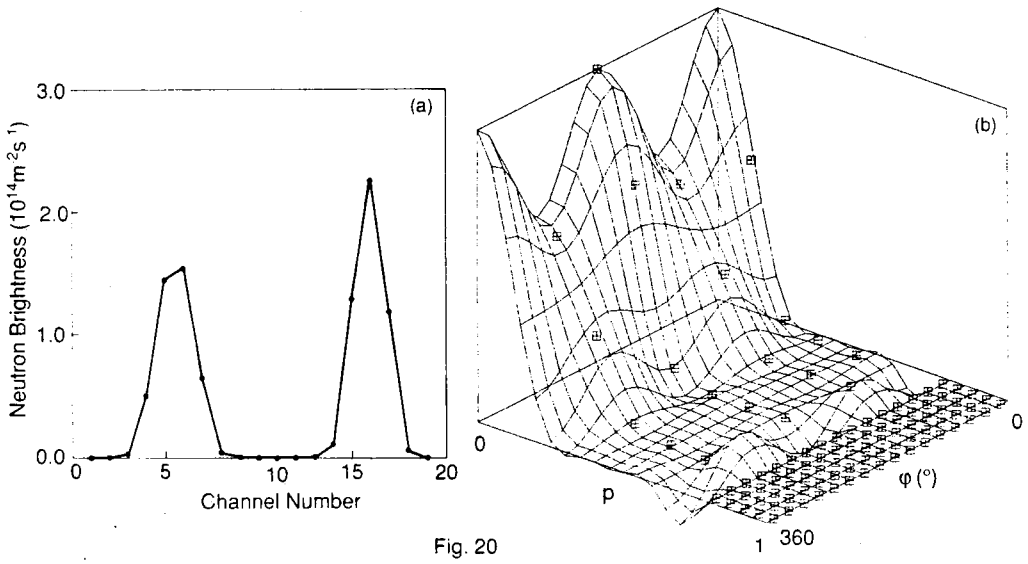

Fig. 20

20. Least-square fit to the second, perturbed peaked artificial brightness profile using the Cormack Tomography method.

a) Artificial data vs channel number and fit.

b) Same fit in the 2-dimensional (p,φ) space. Large edge oscillations appear in the fitted profile as a consequence of the random perturbation of the brightness data.

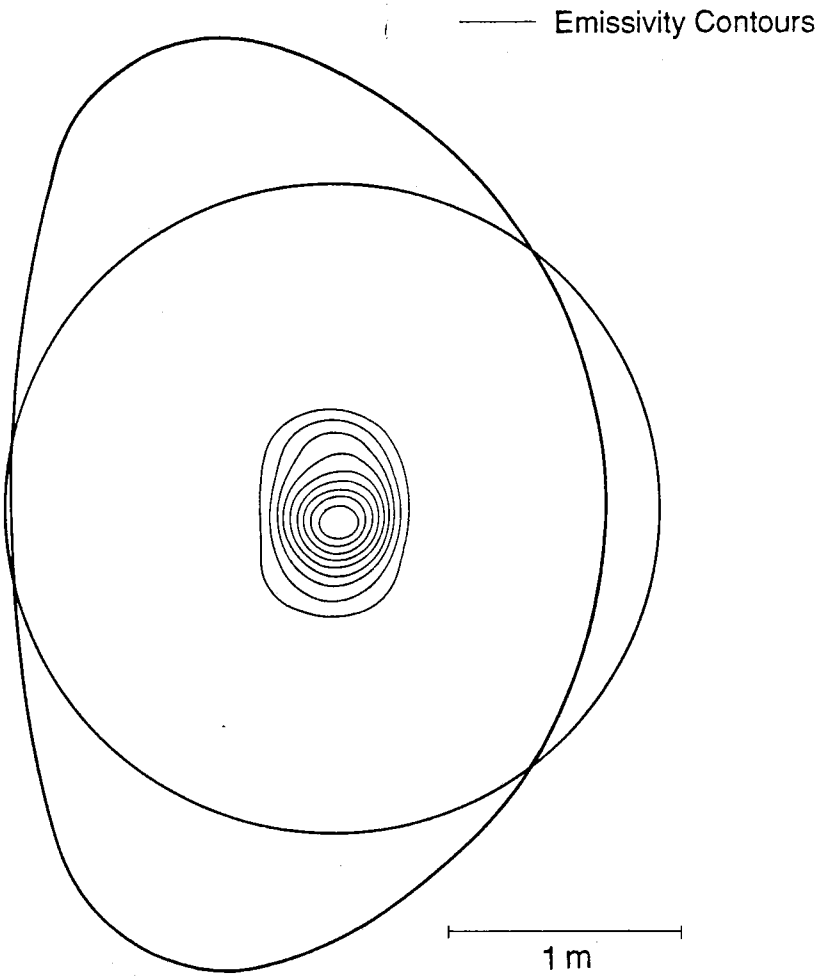

Fig. 21

21. Emissivity topology determined by Cormack Tomography of a perturbed peaked artificial brightness profile. The test profile used here was obtained with a random perturbation of the data of Fig.16a different from the one shown in Fig.20a. We present it here as a better example of distortion of the result of the Cormack Tomography due to uncertainties in the input data.

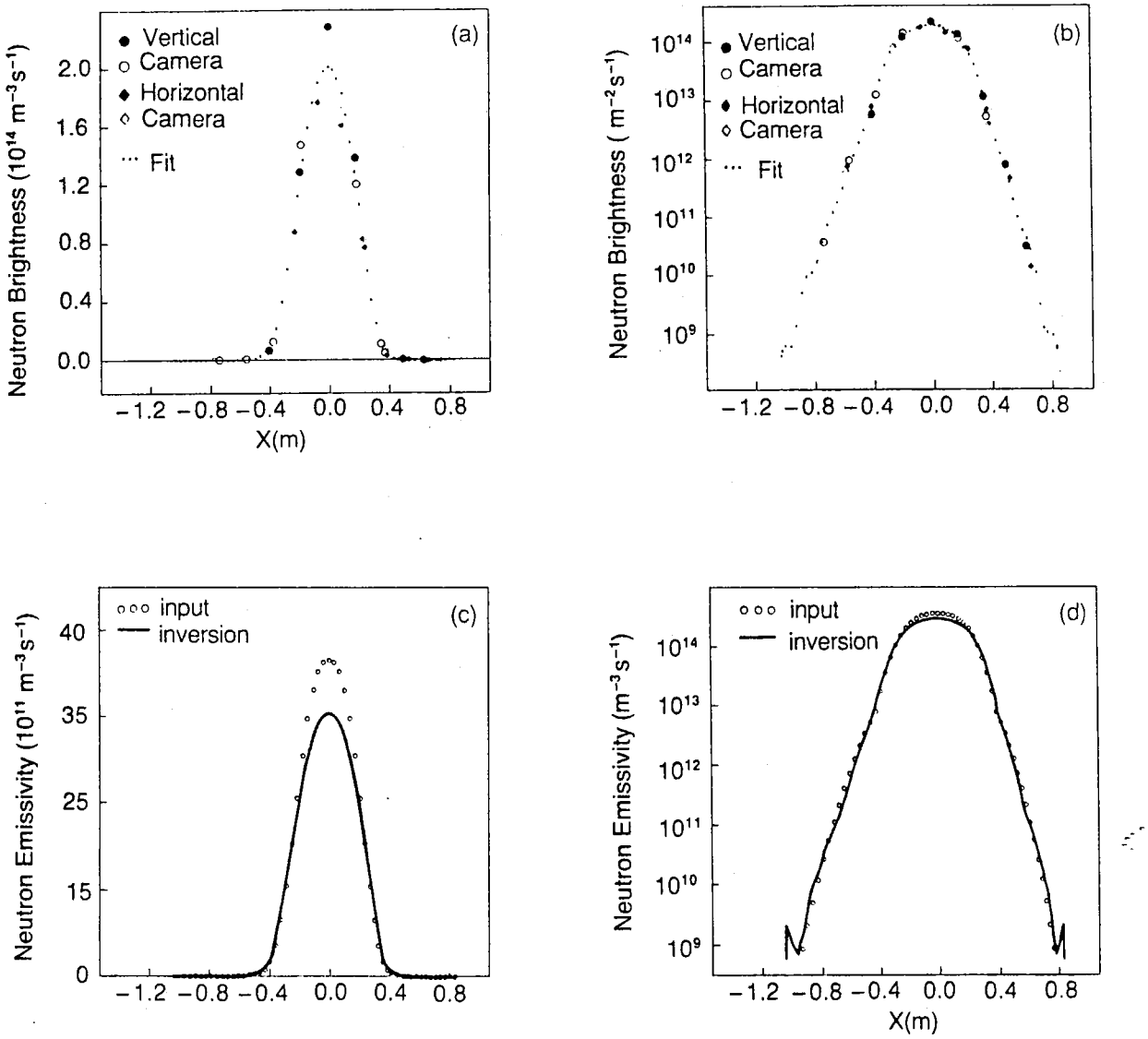

Fig. 22

22. Generalized Abel Inversion of the second peaked artificial profile.

a) Fit of the projected brightness data.

b) Same as a) but using a log scale for the y-axis.

c) Resulting emissivity profile and input profile (linear scale).

d) Resulting emissivity profile and input profile (log scale). This result shows that the result of the Generalized Abel Inversion is only moderately sensitive to the uncertainties in the input data.

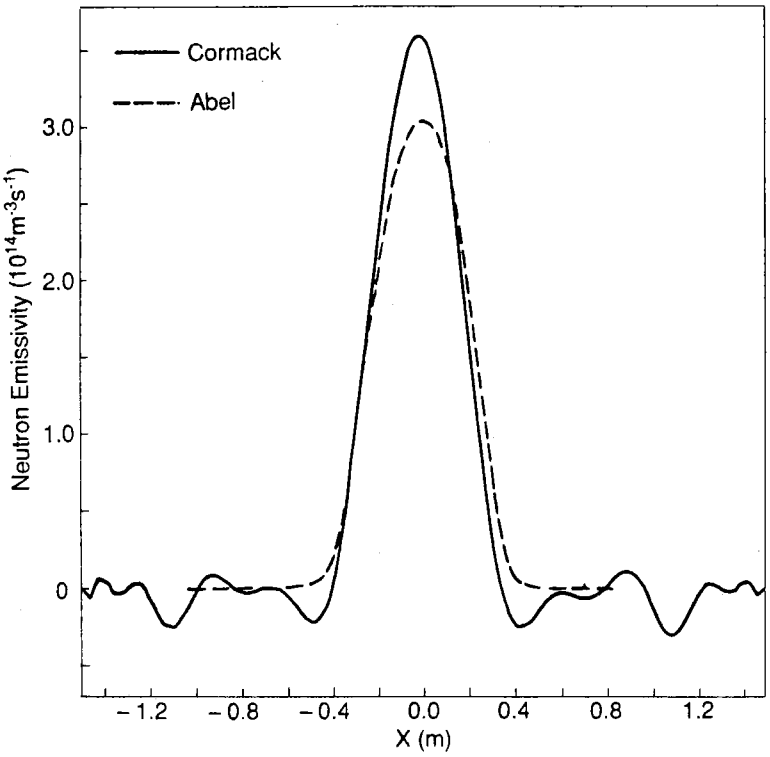

Fig. 23

23. Neutron emissivity profiles on the equatorial plane as determined by Cormack Tomography (full line) and by Generalized Abel Inversion (dashed line) of the second peaked artificial profile.

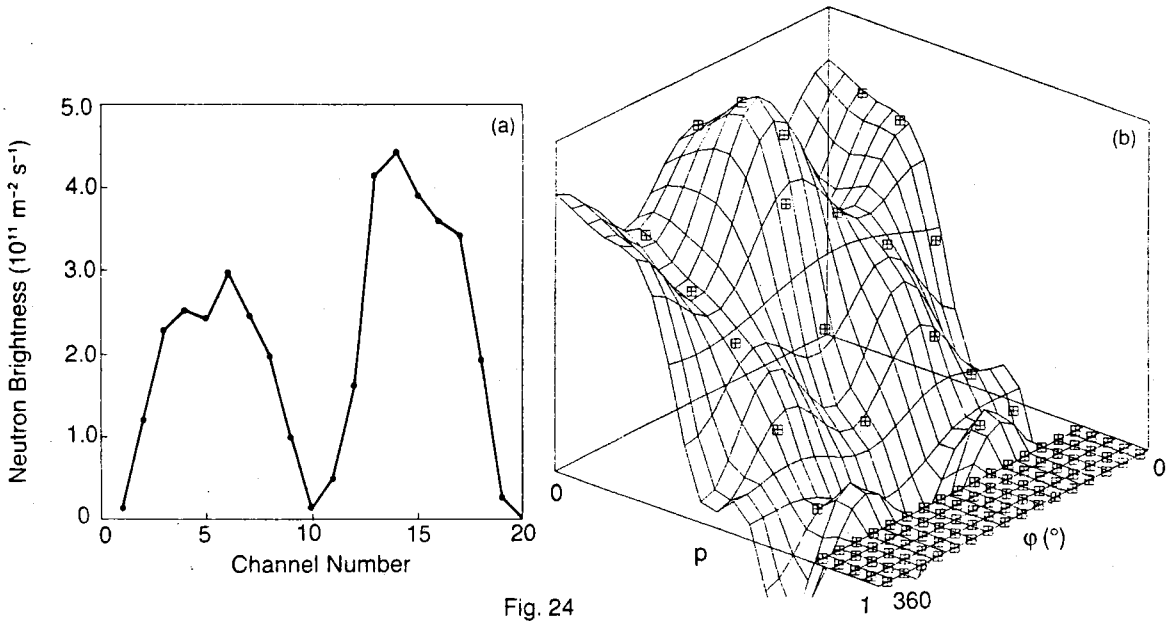

Fig. 24

24. Least-square fit to the broad experimental brightness profile of Fig.3b using the Cormack Tomography method.

a) Fit of the data vs channel number.

b) Same fit in the 2-dimensional (p,φ) space. The large oscillations of the fitted profile are clearly unrealistic.

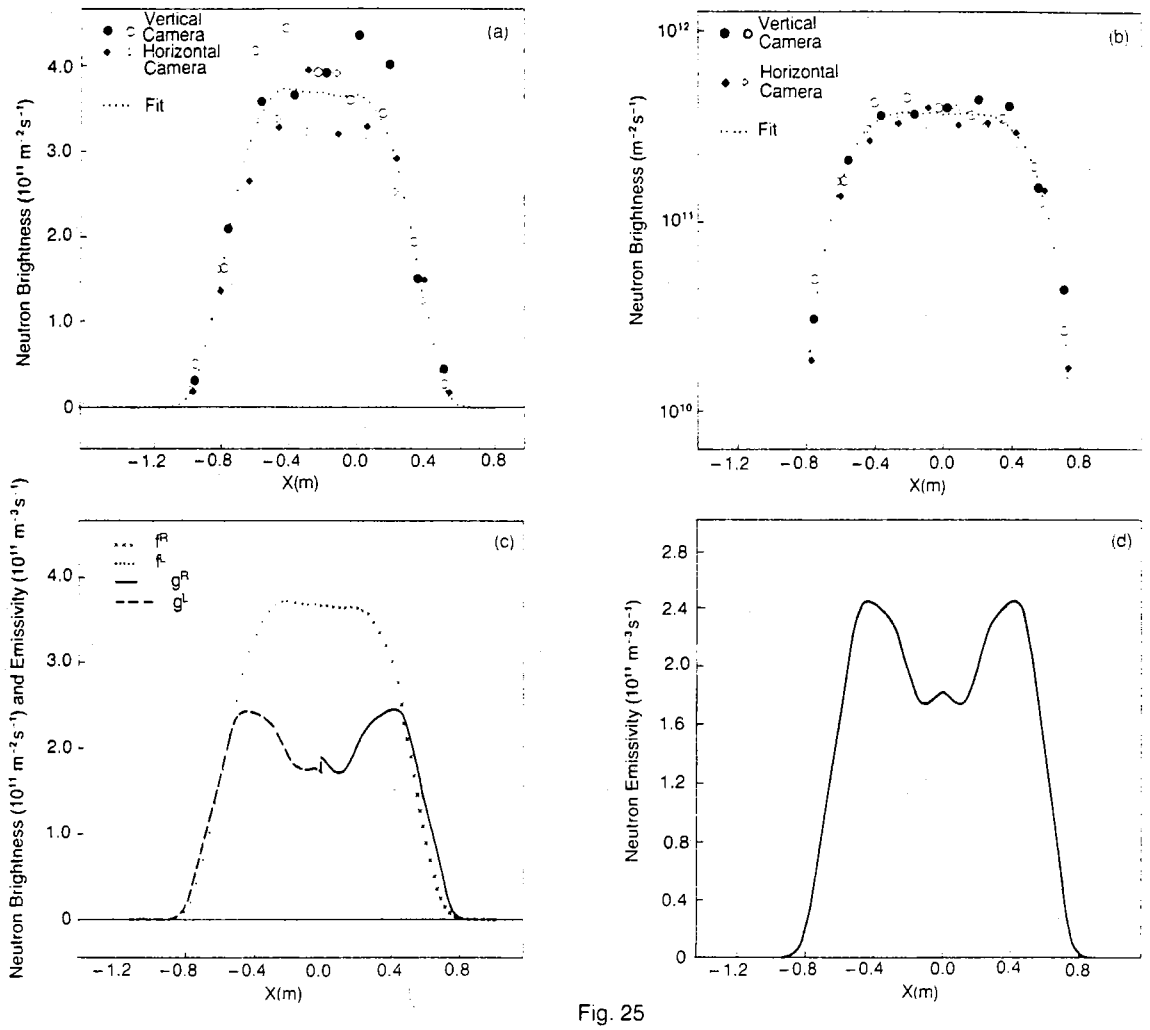

Fig. 25

25. Generalized Abel Inversion of the neutron brightness profile of Fig.3b.

a) Polynomial fit of the projected brightness data. The experimental uncertainties are the main cause for the scatter of the data which is considerable in the central part of the profile. For this case the magnetic flux surfaces of Fig.1 were shifted by 5 cm in order to obtain consistency between the brightness measurements and the magnetic topology.

b) Same as a) but using a log scale for the y-axis.

c) Fitted brightness profiles (f^R and f^L) and corresponding emissivity profiles (g^R and g^L).

d) Neutron emissivity profile obtained by averaging g^R and g^L.

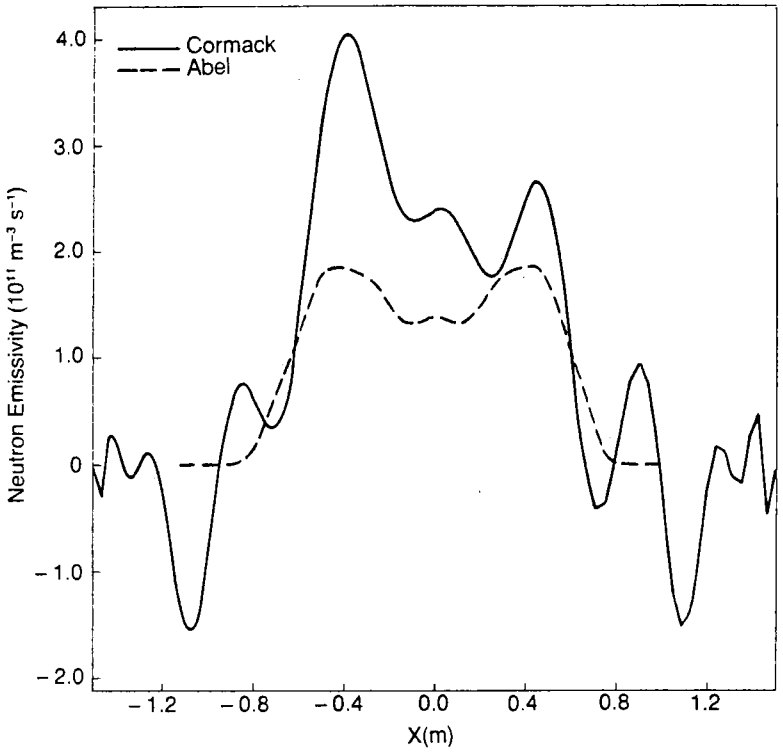

Fig. 26

26. Neutron emissivity profiles on the equatorial plane as determined by Cormack Tomography (full line) and by Generalized Abel Inversion (dashed line) of the brightness profile of Fig.3b. The result of the Cormack Tomography is clearly unacceptable.

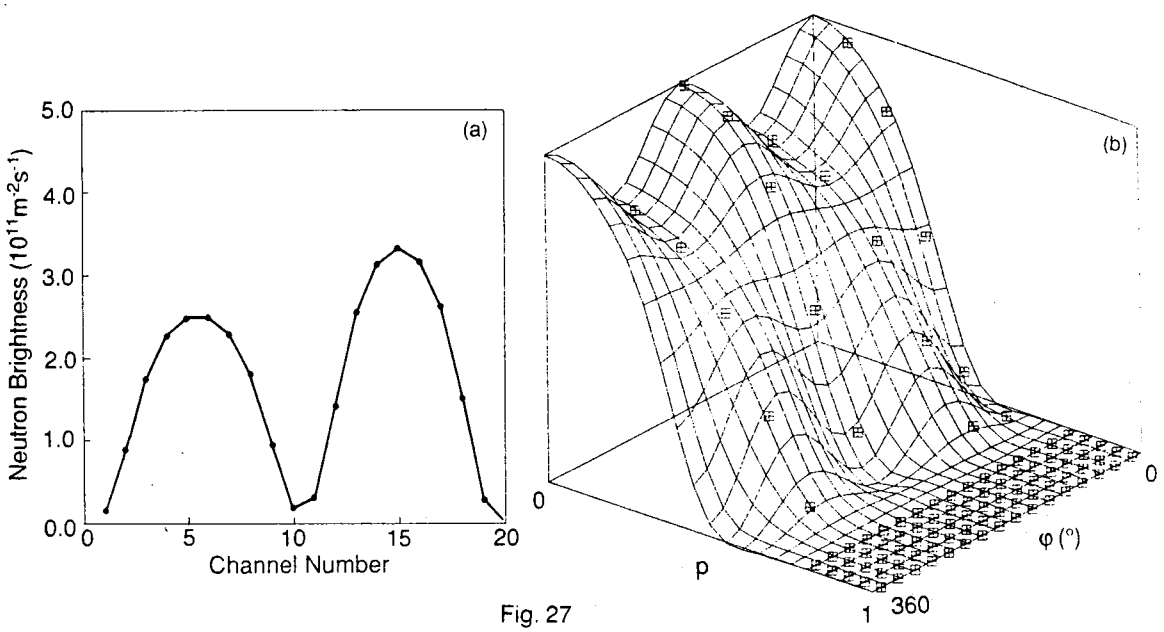

Fig. 27

27. Least-square fit to the first broad artificial brightness profile using the Cormack Tomography method.

a) Artificial data vs channel number and fit.

b) Same fit in the 2-dimensional (p,φ) space.

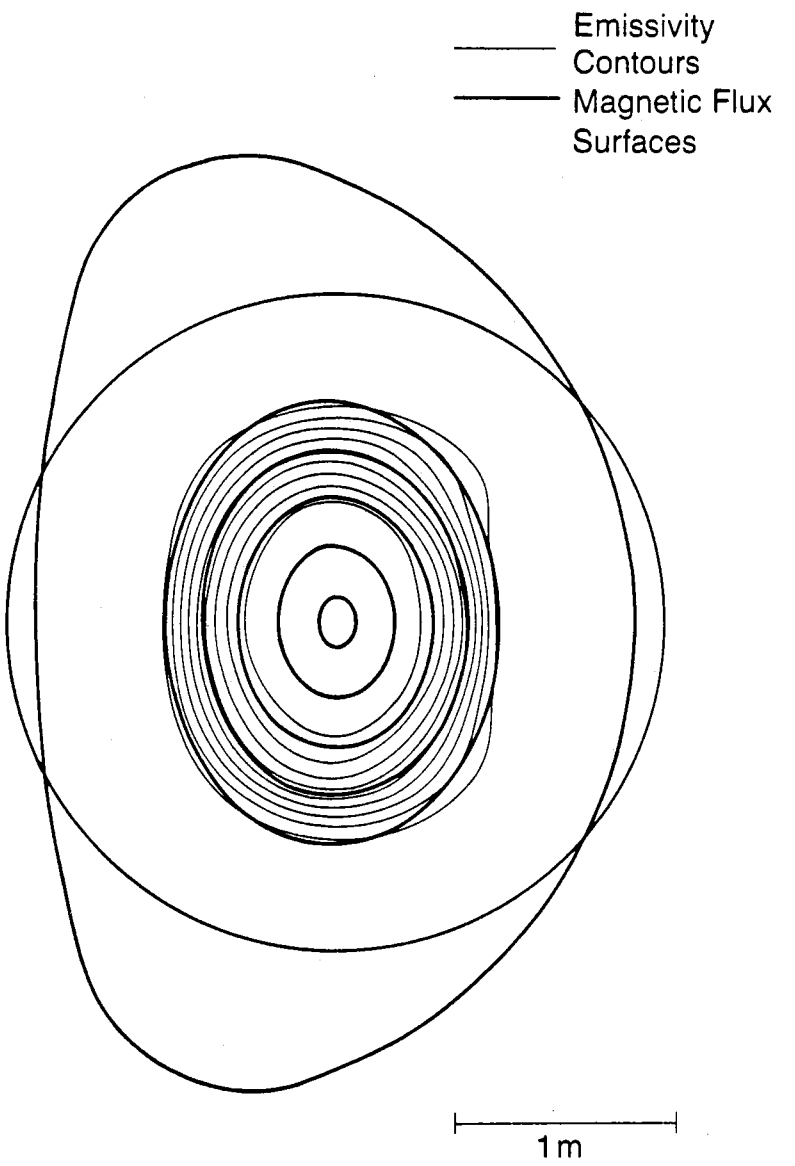

Fig. 28

28. Emissivity topology as determined by Cormack Tomography of the first broad artificial brightness profile. The agreement between the tomography result and the original topology (magnetic flux surfaces) is good.

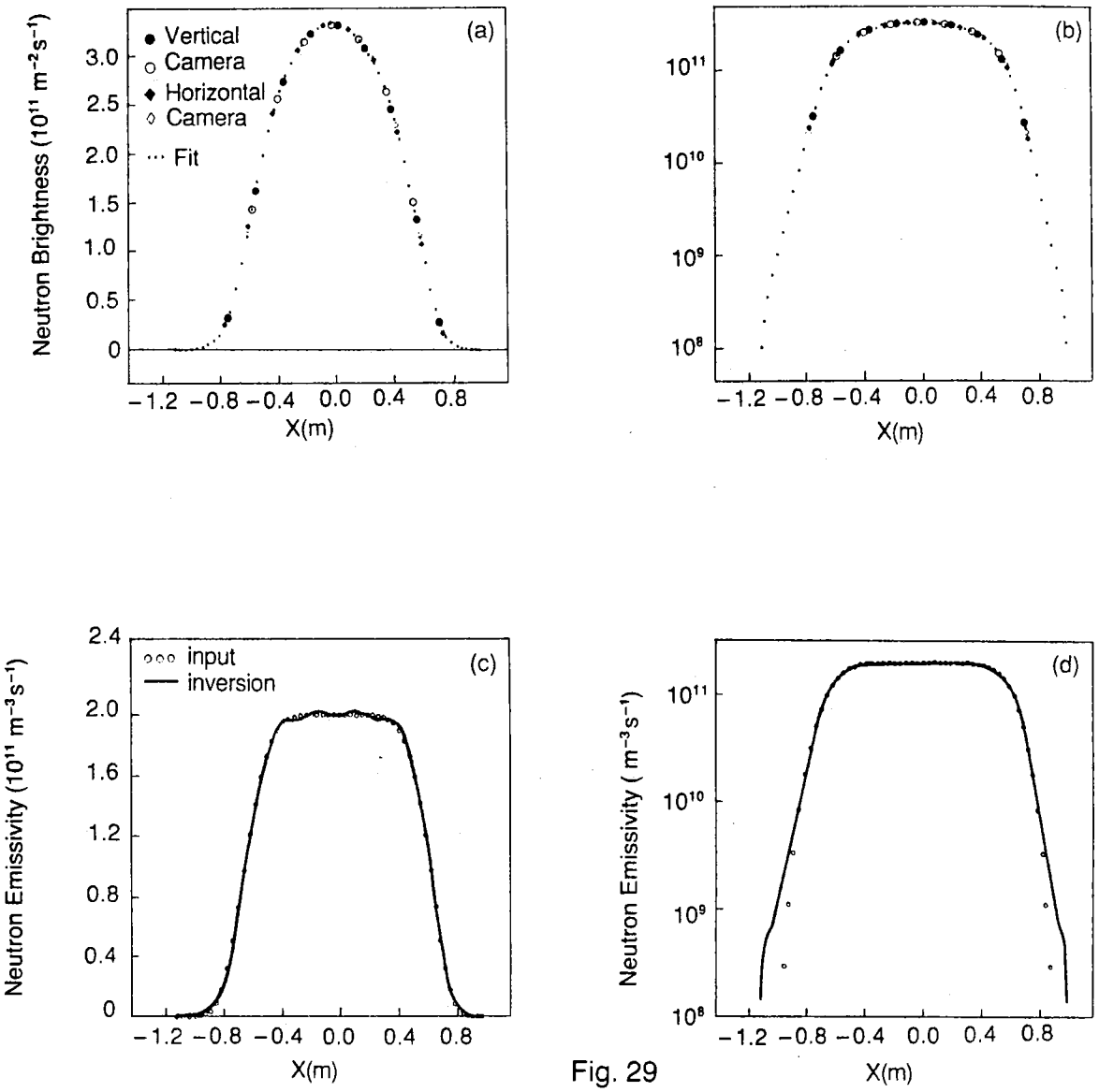

Fig. 29

29. Generalized Abel Inversion of the first peaked artificial profile.

a) Fit of the projected brightness data.

b) Same as a) but using a log scale for the y-axis.

c) Deduced emissivity profile and original profile (linear scale).

d) Deduced emissivity profile and original profile (log scale). In this case the validity of the inversion is limited by the spatial range of the brightness measurements.

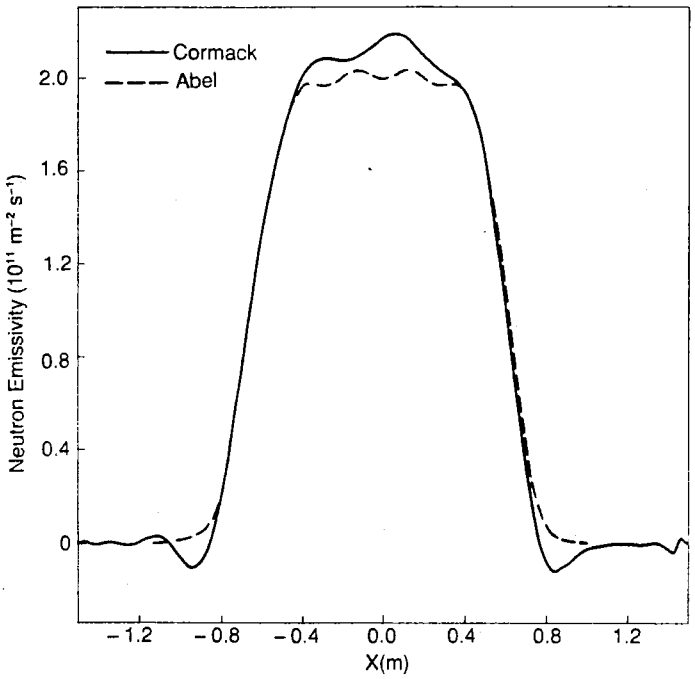

Fig. 30

30. Neutron emissivity profiles on the equatorial plane as determined by Cormack Tomography (full line) and by Generalized Abel Inversion (dashed line) of the first broad artificial profile. The agreement between the two results is good.

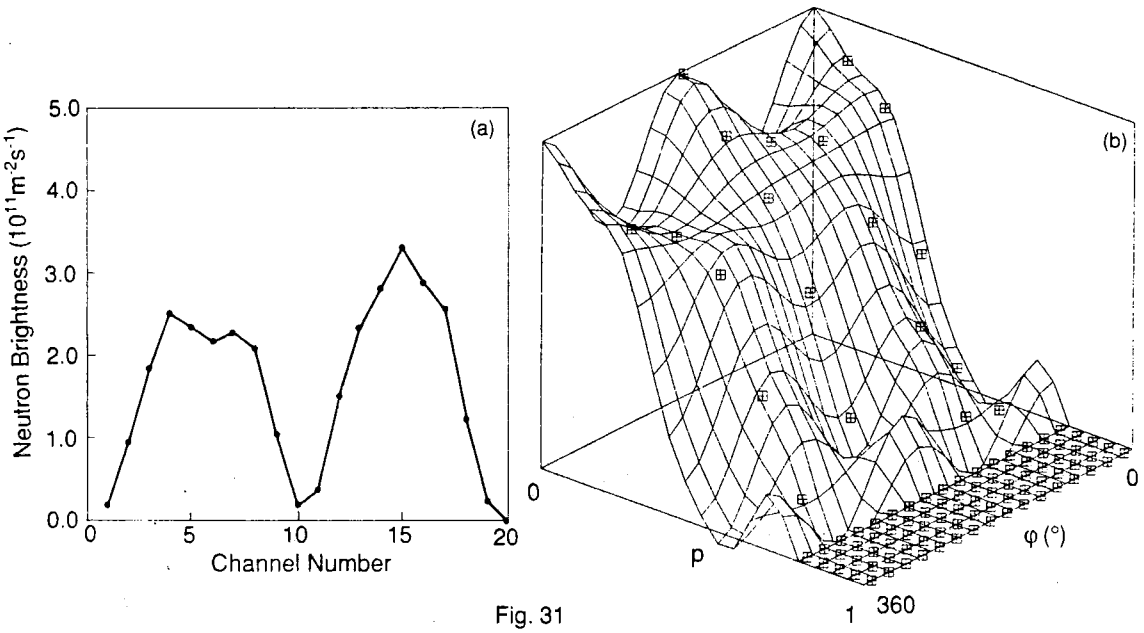

Fig. 31

31. Least-square fit to the second, perturbed broad artificial brightness profile using the Cormack Tomography method.

a) Artificial data vs channel number and fit.

b) Same fit in the 2-dimensional (p,φ) space. The oscillations appearing in the fitted profile are not acceptable.

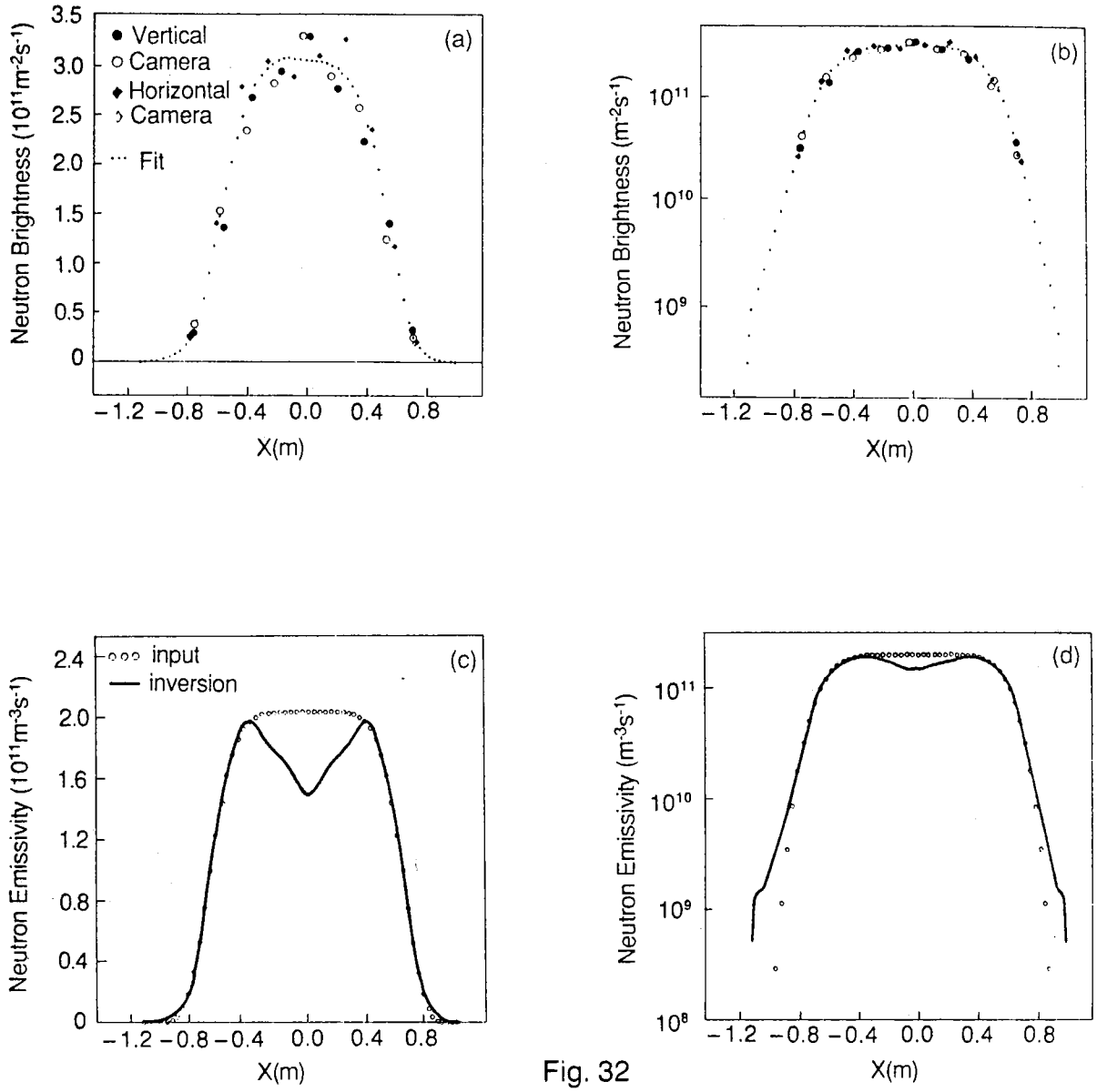

Fig. 32

32. Generalized Abel Inversion of the second broad artificial profile.

a) Fit of the projected brightness data.

b) Same as a) but using a log scale for the y-axis.

c) Deduced emissivity profile and original profile (linear scale). The hollowness of the resulting emissivity profile is entirely a consequence of the perturbation of the input data.

d) Deduced emissivity profile and original profile (log scale).

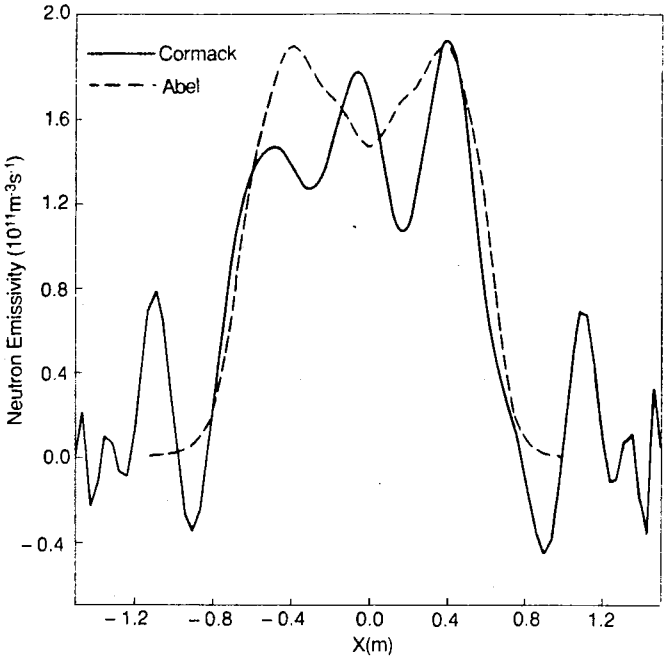

Fig. 33

33. Neutron emissivity profiles on the equatorial plane as determined by Cormack Tomography (full line) and by Generalized Abel Inversion (dashed line) of the second broad artificial profile.

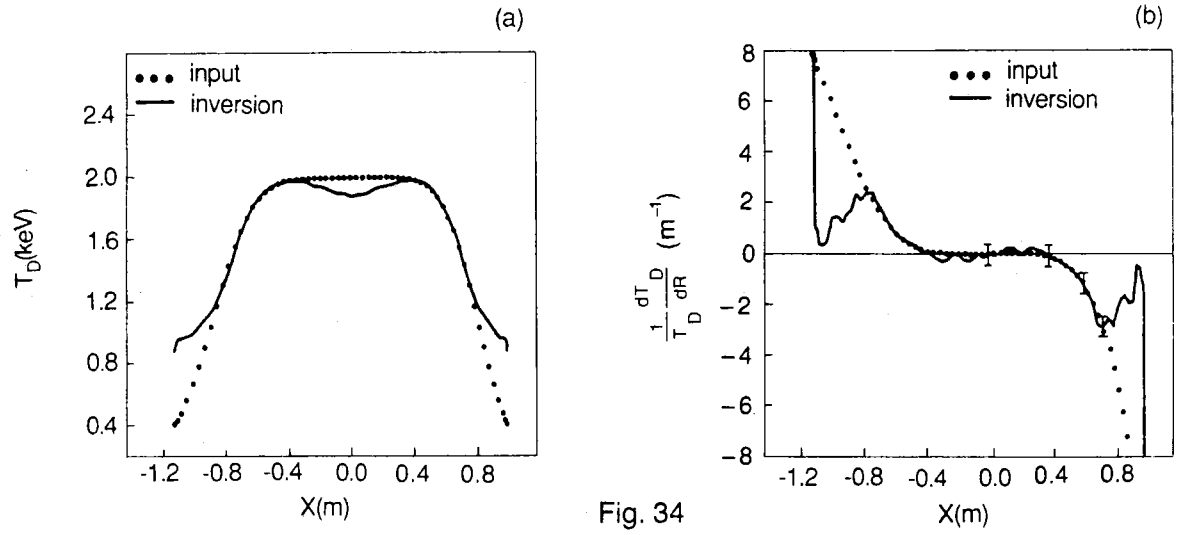

Fig. 34

34.a) Analytical T_D profile relative to the second broad artificial brightness profile (circles) and T_D profile deduced from the corresponding Abel inverted neutron emissivity profile (line). In the spatial range of the brightness data (covering a factor of two variation of T_D) the deduced T_D profile shows an error of ≤10%, which is larger in the central region.

b) Profile of the quantity $1/T_D\ dT_D/dR$ deduced from a). The vertical bars represent an estimate of the uncertainty propagating on $1/T_D\ dT_D/dR$ from random uncertainties in the brightness profile.

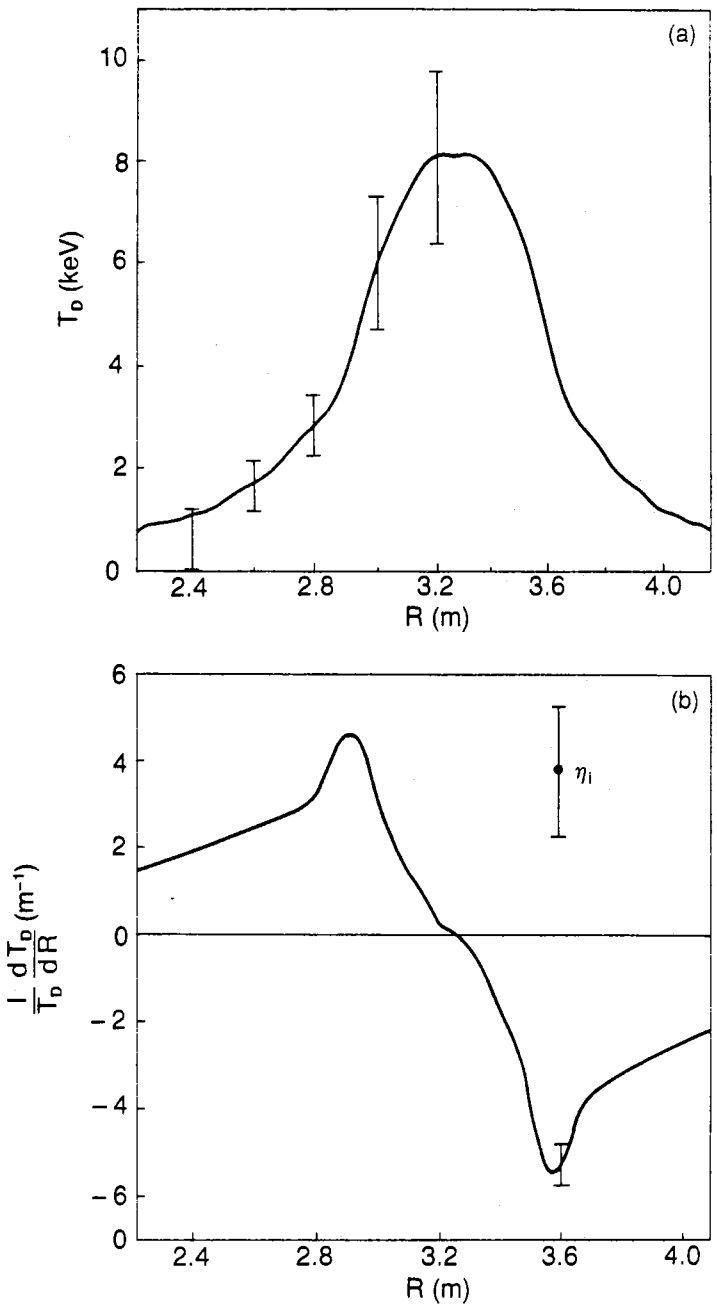

Fig. 35

35.a) T_D profile deduced from the neutron brightness profile of Fig.3a. The error bars (±21%) near the centre of the profile represent the absolute uncertainty on the T_D values. Consistently with the results of Sect.5, outside the spatial range of the measurements the inversion result can be used as an asymptotic upper limit for T_D, as represented by the error bars near the edge of the profile.

b) Profile of the quantity $1/T_D\ dT_D/dR$ as deduced from a). The data have been smoothed to eliminate some small scale oscillations which are an artifact of the analysis. The error bar is ±0.6 m^{-1} . The value of η_i at R=3.6 m is also plotted with its error bar (±40%).

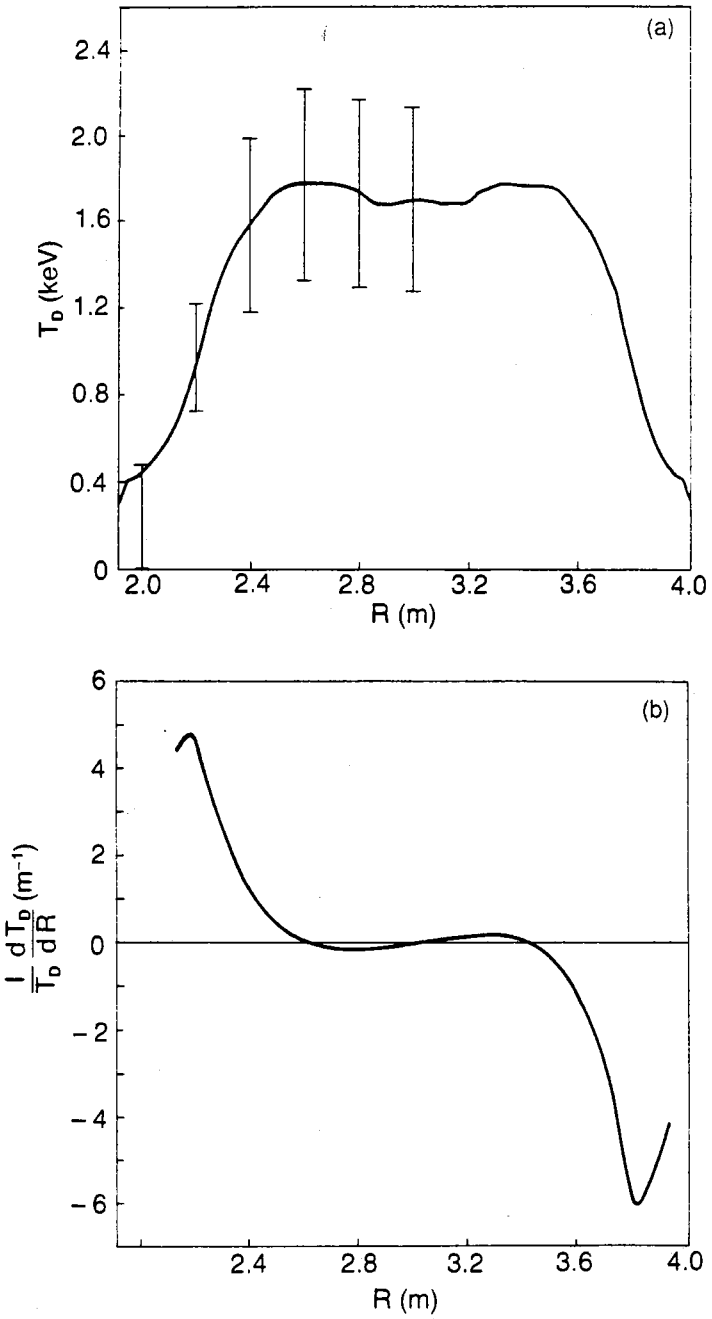

Fig. 36

36.a) T_D profile deduced from the neutron brightness profile of Fig.3b. The larger uncertainty (±25%) in the centre of the profile is due to the higher Z_{eff} value of this plasma discharge.

b) Profile of the quantity $1/T_D\ dT_D/dR$ as deduced from a).

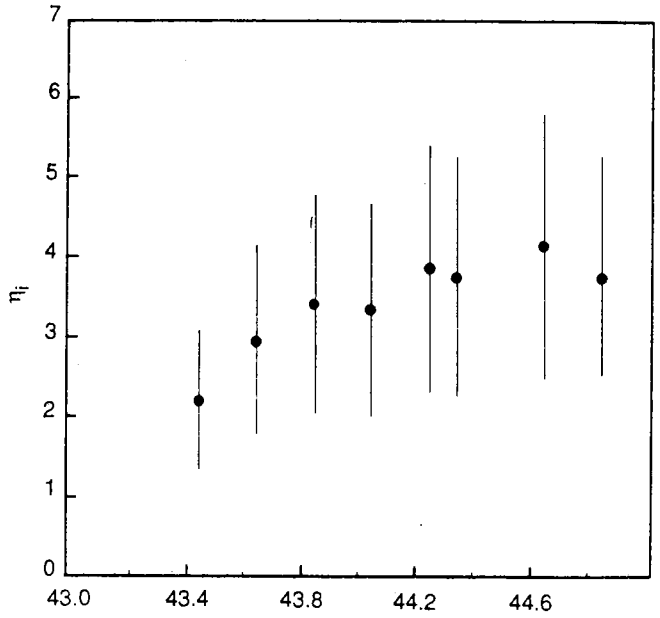

Fig. 37

37. Time evolution of the maximum value of η_i in the interval 3.4<R<3.6 m during the plasma discharge of Fig.4a, as determined by the analysis of neutron brightness measurements.

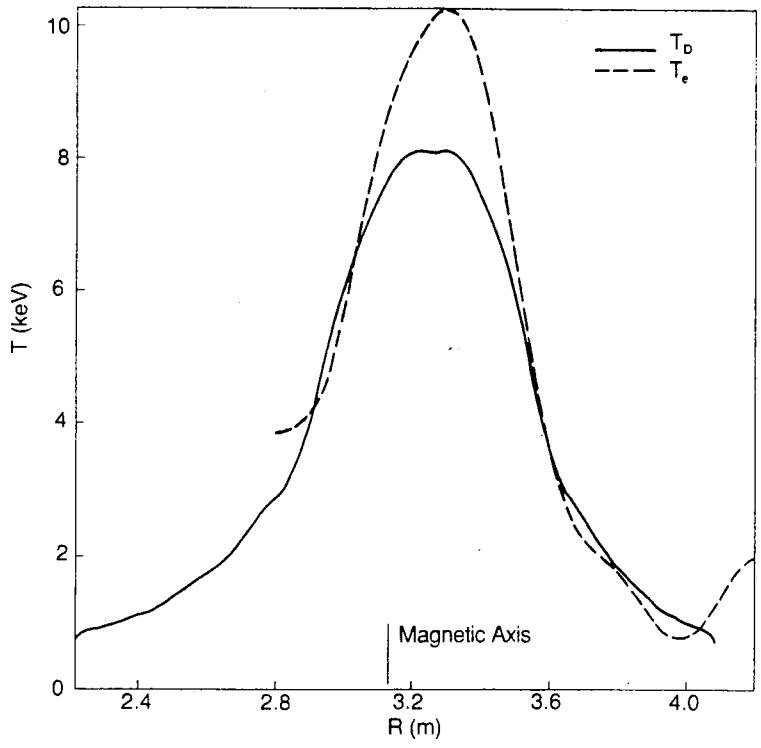

Fig. 38

38. Temperature profiles for JET plasma discharge 16211 at time t=44.25 s. The T_D profile (full line) is the same as in Fig.35a and is averaged over 100 ms. The T_e profile (dashed line) is determined from ECE measurements.

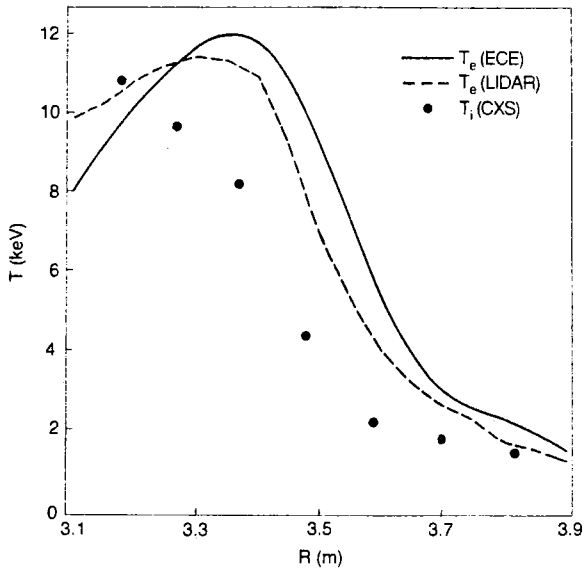

Fig. 39

39. Temperature profiles for JET plasma discharge 17749 at time t=44.2 s. The T_i profile (full circles) is determined from charge exchange spectroscopic measurements of carbon. The T_e profiles are determined from ECE measurements (full line) and LIDAR Thompson scattering measurements (dashed line).

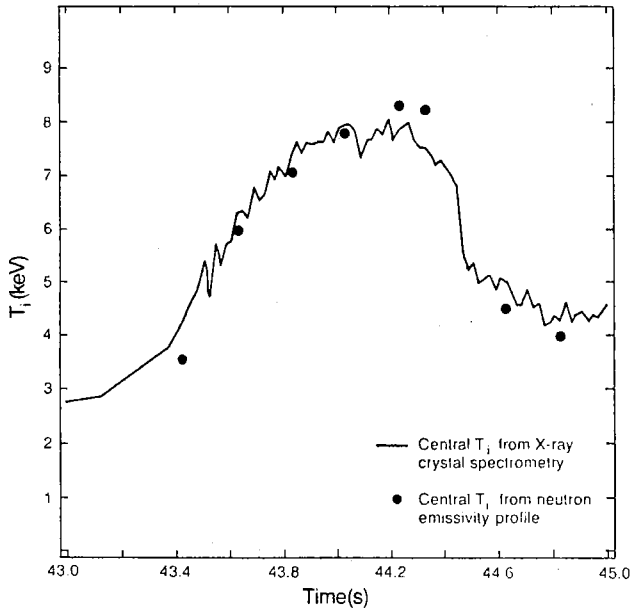

Fig. 40

40. Time evolution of the peak ion temperature during the ICRF heating of JET discharge 16211, following the injection of a 4 mm deuterium pellet at 43.0 s. The circles are the values deduced from neutron brightness measurements, the line is the result of the X-ray crystal spectrometer measurements.

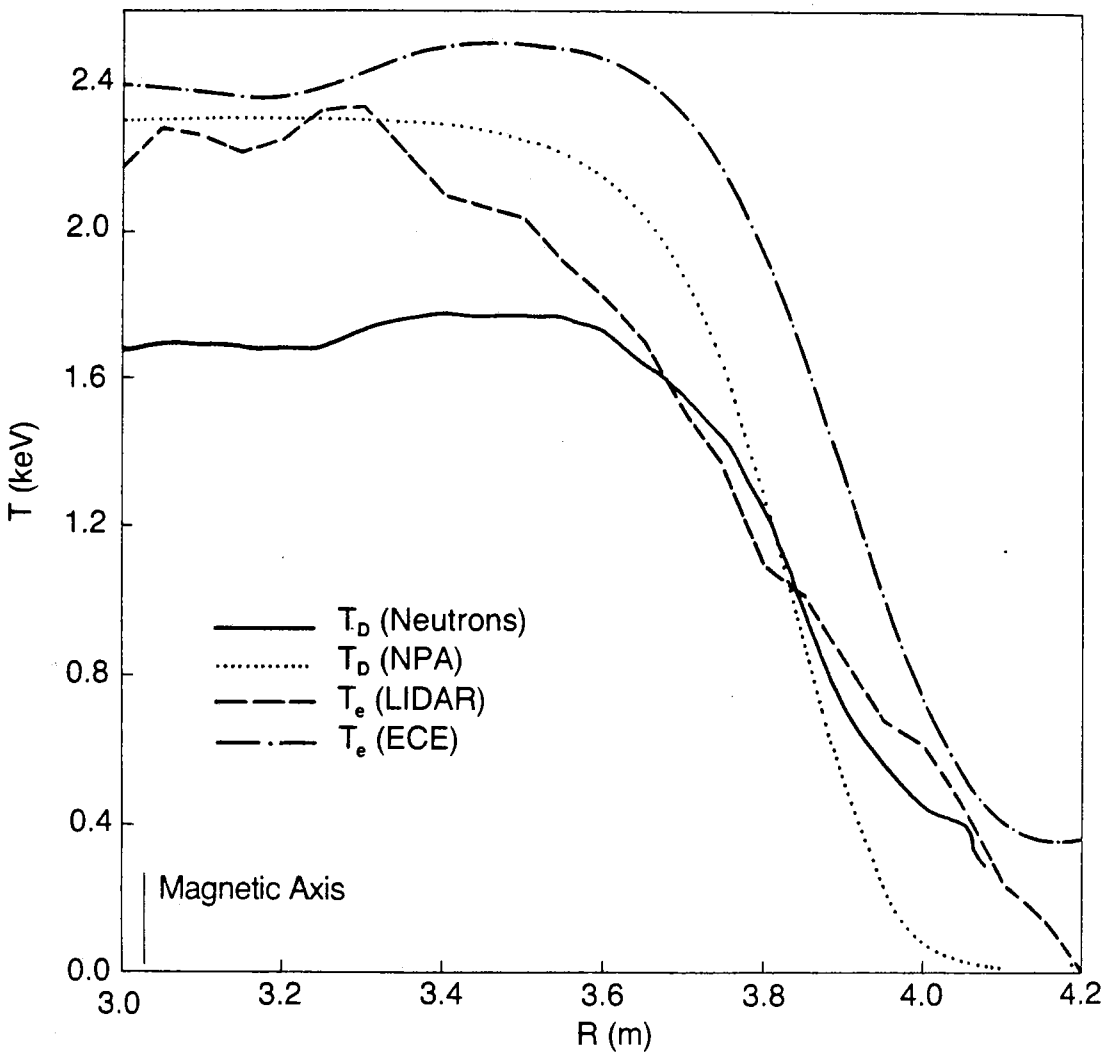

Fig. 41

41. Temperature profiles during the current flat top of JET plasma discharge 13979. The agreement between the T_D profile from the Neutral Particle Analyser (dotted line) and from neutron brightness (full line), and between the T_e profile from ECE (broken line) and from LIDAR (dashed line) is within the uncertainties in the radial position and absolute value of the data points.